INVESTIGATION OF SOLAR VARIABILITY USING SATELLITE MEASUREMENTS OF THE MGII INDEX

MASTER THESIS

By
Shakeri, Farhad
(Mat. No. 2354891)

INSTITUTE OF
ENVIRONMENTAL PHYSICS (IUP)

POSTGRADUATE PROGRAMME ENVIRONMENTAL PHYSICS (PEP)
UNIVERSITY OF BREMEN (FB1), BREMEN, GERMANY

July, 2010

SUPERVISOR: *PD Dr. Christian von Savigny*

REFEREE: 1. PD Dr. Christian von Savigny
2. Dr. Mark Weber

Declaration

I herewith declare that I did the written work on my own and only with the means as indicated.

date and signature

Acknowledgements

This research project would not have been possible without the support of many people. My first appreciation is for the IUP faculty for the impetus imparted to me during the course works and also for the PEP coordinators and staff; Prof. Dr. John Burrows, PD Dr. Annette Ladstätter-Weißenmayer, Mr. Lars Jeschke and Mrs. Anja Gatzka, for providing the students such a wonderful atmosphere to study and for kindly devoting themselves to this master program.

I owe my deepest gratitude to my supervisors, PD. Dr. Christian von Savigny and Dr. Mark Weber who were abundantly helpful and offered invaluable and endless assistance, support and guidance in all the time of research and writing of this thesis. I am grateful for their patience, motivation and enthusiasm.

Special thanks also to all my graduate friends, especially Benjamin Sampson and Sarfraz Sikandar for all the unforgettable times we had, to my colleagues Katja Weigel and Faiza Azam for their helps and advices and to my best friends Alireza Sadeghi and Amir Jafari for their continued and invaluable support.

Most importantly, I wish to express my love and gratitude to my beloved family to whom this master thesis is dedicated; my father, my mother and my brother, who have always been there for me whenever I needed them and supporting me spiritually every second of my life. And Finally, I would like to express my heartfelt gratitude to the love of my life, Shabnam, for her support and endless love, which has been my source of strength and inspiration through the duration of my study.

Table of Contents

Introduction

The major source of the energy which affects Earth's atmosphere is the Sun. The energy emitted by the sun passes through space until it is intercepted by the Earth. Only about 40% of the solar energy received at the top of Earth's atmosphere passes through to the surface. Roughly 30% of the sun's visible radiation is reflected back to space by the atmosphere or the Earth's surface. A great amount of incoming radiation especially in ranges of ultraviolet and infrared is absorbed by the atmosphere. For instance, most of the solar ultraviolet radiation with a range of wavelengths from 200 to 300 nm is absorbed by ozone (O3) gas in the stratosphere. The energy absorbed by the surface is then re-emitted back to the space in form of long-wave radiation; however a significant portion of this re-emitted radiation will be absorbed by the atmosphere in a process known as greenhouse effect.

In general, the balance between absorbed and radiated energy determines the average temperature. This radiation balance can be altered by the variations in solar energy reaching the earth.

For general purposes, the energy output of the sun can be considered to be constant. This of course is not entirely true. Due to cyclic behavior of the magnetic field of the sun, there are periods of time that sun is more active and so the output solar irradiance is slightly enhanced. From the other hand, there are also periods of time in which the sun is more quite and therefore the total solar irradiance is getting moderated. The period of this cyclic behavior is 11 years. In addition, the rotational period of the sun which is approximately 27 days and its higher order harmonics like 13.5 and 9 day harmonics are also important in terms of fluctuations in incoming solar irradiance to the Earth's atmosphere. The photochemistry of the atmosphere, from the other hand, is highly sensitive to the incoming ultraviolet radiation. The variation in total solar irradiance through each 11-year solar cycle is roughly 0.1% (for all wavelengths), while the variation in UV flux can be as high as 100%. The effects of 11-year solar cycle on Earth's atmosphere have been investigated for a long time and by many scientists. There are also some atmospheric processes with short-term periodic variability which is believed to be consequences of rotation of the sun. Anomalous ozone response in the upper stratosphere to 27 day rotational period and its 13.5 day harmonic in UV flux, short-term periodic variations in stratospheric temperature by 0.5 K, evidences of 27 and 13.5 day solar signature in noctilucent clouds occurrence frequency and 27 day periodic variations in cloud amount on equatorial pacific ocean are examples of these short-term periodic signatures occurring in the Earth's atmosphere.

Based on these facts, study of the short-term periodic cycles of incoming solar irradiance in UV region seems to be crucial in terms of atmospheric processes.

This master thesis is devoted to the study of variations in ionized magnesium doublet emission lines "Mg II" at 280 nm in the solar spectrum, which has been found to be a convenient proxy for monitoring the variations in UV flux and contain information on the temperature fluctuations that occur in the chromosphere during the solar cycles. The main objectives of this study are producing a long-term trend of magnesium II index from 1978 to 2010 and looking for short-term periodic signatures in total composite. The time series used in this work have been provided by various space based instruments such as "SCanning Imaging Absorption spectroMeter for Atmospheric CHartographY" (SCIAMACHY), "Global Ozone Monitoring Experiment" (GOME) and "Solar Backscatter Ultraviolet Radiometer" (SBUV).

Chapter 1 : The Sun

1.1. General Knowledge

According to a theory proposed by Laplace (1796), the sun condensed out of the center of a thin, hot, spinning disk of interstellar material about 4.6 billion years ago. Among the billions of stars in the universe, the sun is an average star in mass but below average in size. The unique feature of the sun for us is that it is 300,000 times closer to the earth than the next nearest star. The mean distance between the earth and the sun is about 1.5×10^{8} km. Virtually all of the energy that the earth receives comes from the sun. This is the energy that sets the earth’s atmosphere and oceans in the motion.

The sun is a gaseous sphere with a radius of about 6.96×10^{5} km and a mass of approximately 1.99×10^{30} kg. Its main ingredients are primordial hydrogen (H) and helium (He), plus a small amount of heavier elements including oxygen (O), carbon (C), nitrogen (N), neon (Ne), iron (Fe), silicon (Si), magnesium (Mg), sulfur (S), and calcium (Ca). Hydrogen makes up roughly 90% of the mass, and the remaining 10% or so is helium. The temperature of the sun decreases from a approximately 5×10^{6} K at the central to about 5800 K at the surface. Also the density of the sun falls off very rapidly from the center to the surface. The central density is about 150 g/cm^3, and at the surface, it is about 10^{-7} g/cm^3. However the average density is about 1.4 g/cm^3. Roughly about 90% of the sun’s mass is contained in the inner half of its radius.[1]

Solar energy is generated by the conversion of four hydrogen atoms to one helium atom in fusion reactions, which take place in the deep interior of the sun with temperatures up to many millions of degrees.

The Sun's lifetime is about 10 billion years. After this time the hydrogen in the core of the sun will be depleted. The Sun will then become bigger and convert into a very large gaseous sphere called the Red Giant, devouring Mercury and Venus and.

The most important characteristic of the Sun is that it emits huge amount of electro-magnetic radiation of all wavelengths. The total output of the Sun is $3.99\text{x}10^{26}$ W. Only 1.74×10^{17} W strikes the Earth. If we divide this quantity of radiation to the surface of the earth’s disk which is perpendicular to the radiation rays, we come to the amount of 1368 W/m^2 which called the solar constant.

The sun is not a solid body, meaning that different parts of it can have different rotational speed. At the equator the surface rotates once every 25.4 days, while the regions near the poles make a rotation roughly every 36 days. The way that the sun’s surface oscillates, suggest that inner part of the sun spins like a solid object, with a rotational period of 27 days.[2] (figure 1.1)

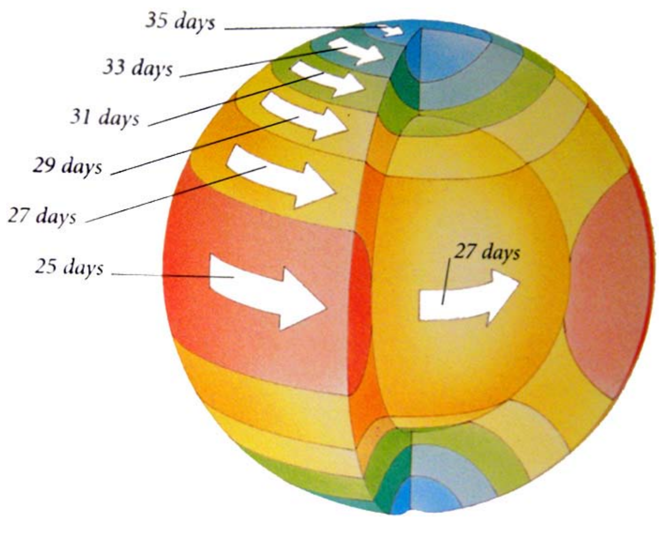

Fig. 1.1. Differential rotation of the sun
Credit: Space encyclopedia

1.2. Structure of the Sun

The Sun is divided into six regions based on the physical characteristics of these regions. The boundaries are not sharp.

- core - region of energy generation
- radiation zone - the region where energy transport is by radiation flow
- convection zone - the region where energy transport is by convection cells
- photosphere - the surface where photons are emitted
- chromosphere - the atmosphere of the Sun
- corona - the superhot region where the solar wind originates

The structure of the Sun as a series of concentric spherical shells, or zones, is illustrated in figure 1.2. These zones have different physical characteristics, as deduced from observations and the theoretical development of the standard solar model.

The inner zone or core is the region that generates the energy by nuclear fusion. The other regions of the sun are heated by energy that is transferred outward from the core. All of the energy produced in the core travels through successive shells to the solar photosphere before it escapes into space as sunlight or kinetic energy of particles.

Followed by the core is the Radiative zone. In this zone there is no thermal convection. The material in these zone gets cooler as altitude increases (from 7,000,000 K to about 2,000,000 K)[3]. This temperature gradient is less than the value of adiabatic lapse rate and hence cannot derive convection. The Heat transfer is happened by radiation; ions of hydrogen and helium emit photons, which travel only a short distance before being reabsorbed by other ions. The density drops sharply from the bottom to the top of the radiative zone.

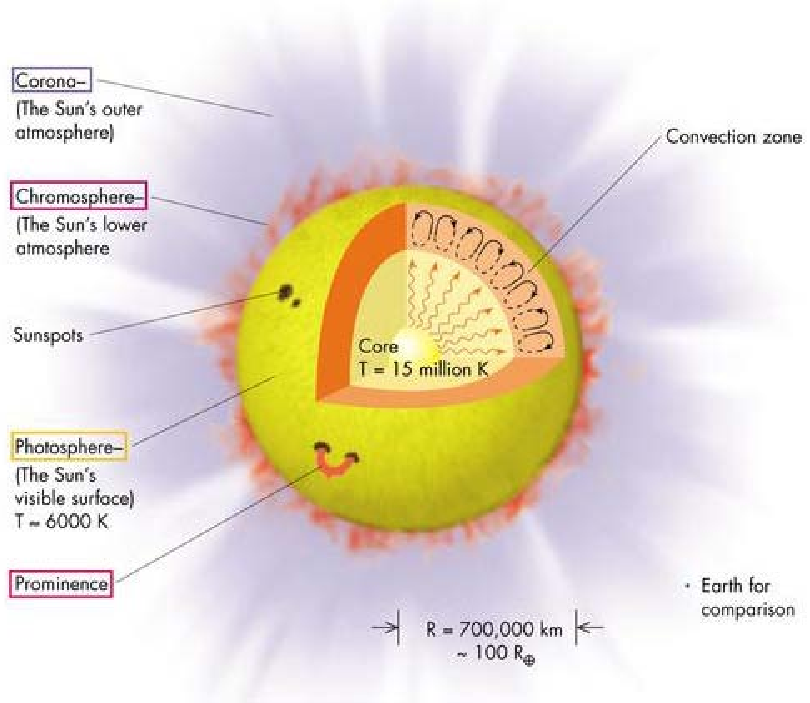

Fig. 1.2. A cross section of the sun illustrating the solar interior and atmosphere.
Credit: Bryan J. Méndez, Space Sciences Laboratory, University of California, Berkeley

In Convection Zone, the solar plasma is not hot or dense enough to transfer the heat energy via radiation. As a result, thermal convection occurs as thermal columns carry hot material to the surface (photosphere) of the Sun.

The photosphere is the visible surface of the Sun. In fact this is not a solid surface but a very thin layer of gas of about 100 km thickness. When we look down to the sun, the view becomes more and more opaque. The point where it appears to become completely opaque is the photosphere. Thus, the photosphere may also be defined as the imaginary surface from which the solar light appears to be emitted. Below the photosphere the amount of hydrogen ions, which absorbs visible light, is relatively higher than above regions, and this makes the upper layers being transparent to visible light.

Above the photosphere lies the solar atmosphere that has three distinct regions:

- The cool chromosphere, sometimes called the color sphere and can be seen in total eclipse.
- The transitional region in which the temperature rises rapidly to 8000 K.
- The low-density, hot corona at a temperature of 10^6 K. The expansion of the corona into the interplanetary medium (IPM) becomes the solar wind, which extends millions of kilometers throughout the solar system.

Region	Thickness	Temperature
core	0.3 solar radii	$15x10^6$ K
radiation zone	0.3-0.6 solar radii	$6x10^6$ K
convection zone	0.6-1.0 solar radii	$1x10^6$ K
photosphere	100 km	6000 K
chromosphere	2000 km	30,000 K
corona	10^6 km	$1x10^6$ K

Table 1. The Structure of the Sun

1.3. Sun's Interior and Energy Source [4],[5]

The interior of the sun governed by 5 different relations or physical concepts:

1. *Hydrostatic equilibrium - the balances between pressure and the self-gravity*

the sun is not expanding or contracting, therefore it is in equilibrium. This means that the inward force of gravitation balances with outward force of pressure.

2. *Thermal equilibrium - the amount of energy generated inside must be equal the amount of energy radiated to the outer space*

If the energy produce is increased, the temperature and the pressure will be increased too. So the star expands and the surface area increases and this leads to more radiation of energy to space. This radiation balances the increased energy production.

3. *Opacity - the resistance of the solar envelope to the radiation*

The regions of low density let the photons flow through them easily (low opacity), vice versa, the regions with higher density resist the flow of photons and scatter the radiation (high opacity).

4. *Energy transport - how energy is transported from the core to the surface*

Among the three ways to transfer energy - conduction, convection and radiation - only the two latter ones are important in the Sun and the opacity determines which method is used. Where the temperature is so high, almost all the atoms are stripped of their electrons, the opacity is low and radiation transfer is dominant. In this case the photons travel outward from the regions with high density to the regions with lower density. Typically it takes about 100,000 years for a photon to travel from core to the surface.

On the other hand, where the temperature drops, near the outer layers of the sun interior, the stripped protons and electrons recombine to form atoms and so the opacity is increased, slowing down the energy transfer by radiation. here the convective cells – bubbles - form. These bubbles are hot and have relatively low density. The bubbles rise up to the outer layers and there release their energy. The temperature drops and the density increases again and the bubbles sink; the energy is transferred through a convective loop.

5. Energy production - in the sun like other stars, energy is produced by thermonuclear fusion

The sun like other stars consists mainly of hydrogen and some helium. Only these two elements were produced directly from the Big Bang. Nuclear power is the only source of energy in the Sun. There are two types of nuclear power possible: fusion and fission. Fission generates energy by breaking up massive nuclei. Fusion produces energy by fusing the light nuclei together. So it is logical to conclude that what is responsible for huge amount of energy in the sun is nothing but nuclear fusion.

We know that the hydrogen in the core is positively charged (it is ionized). To get these positively-charged Hydrogen nuclei - or simply protons - to fuse together, their electrical repulsion must be overcome. This can happen at temperatures above 15×10^6 K, where the motions of protons are high enough to overcome the electrostatic force and the nuclei can fuse. At this stage, the distance between two protons is in the order of 10^{-15} meter. Here the strong nuclear force shows up. This force is much more powerful than the electric force and makes the nuclei stick together.

In the cores of the sun, four hydrogen nuclei (protons) are fused together to form a single helium nucleus. The mass of a helium nucleus is 99.29% the mass of four protons, 0.71% of this mass is missing. Putting this quantity of material in Einstein's famous relation $\boldsymbol{E = mc^2}$, we find the enormous source of energy. The efficiency of this reaction is about 0.8%. This energy radiated away in form of high-energy gamma rays. Doing a simple calculation, one can easily noticed that the Sun could last for about 10 billion years on hydrogen fusion in its core.

1.4. Photosphere

The Photosphere is the visible region of the sun, where most of the electromagnetic energy reaching the earth originates. It is a comparatively thin layer about 500 km thick, consisting of glowing gas. The photosphere is marked by relatively bright granules about 1500 km in diameter. The bright granules are uniformly distributed over the surface and are associated with ascending glowing gases in the top layer of the convection zone. The temperature in this layer varies from 8000 K at the bottom of the layer to 4000 K in the upper layer. As mentioned in section 1.2, the photosphere is transparent to radiation. Matching the theoretical blackbody radiation with the measured spectral solar radiation, the best agreement is found for a temperature of approximately 5770 K. This temperature is an average over the temperature range of the photosphere.

1.4.1. Sunspots and Solar Cycles

Sunspots are the dark regions of high magnetic field, which periodically appear on the photosphere. The average size of these regions is about 10,000 km. The spots usually form in groups and may be unipolar, but usually are paired with a neighboring spot. The groups of sunspots stretch for up to 100,000 km (figure 1.3). The life of the sunspots varies from several days up to several weeks, depending on their size. Some of these sunspots live long enough for them to reappear during the course of the sun's 27-day rotation. [3]

Sunspots are usually found in the zone of latitude between 40° (north and south) and the equator, and never appear near the poles. The spots first appear near latitude 27° in both hemispheres. Gradually they travel toward the equator and disappear close to latitude 8◦. The average temperature of the sunspots is between 3700 and 4100 K, so compare to an average temperature of 5700 K for the photosphere, they are relatively cold. This contrast with the surrounding environment makes them visible as dark spots, as the intensity of a heated black body such as photosphere, is a function of temperature to the fourth power. The magnetic field in a sunspot is 0.1T (roughly 1000 times greater than the average photospheric field). [3],[6]

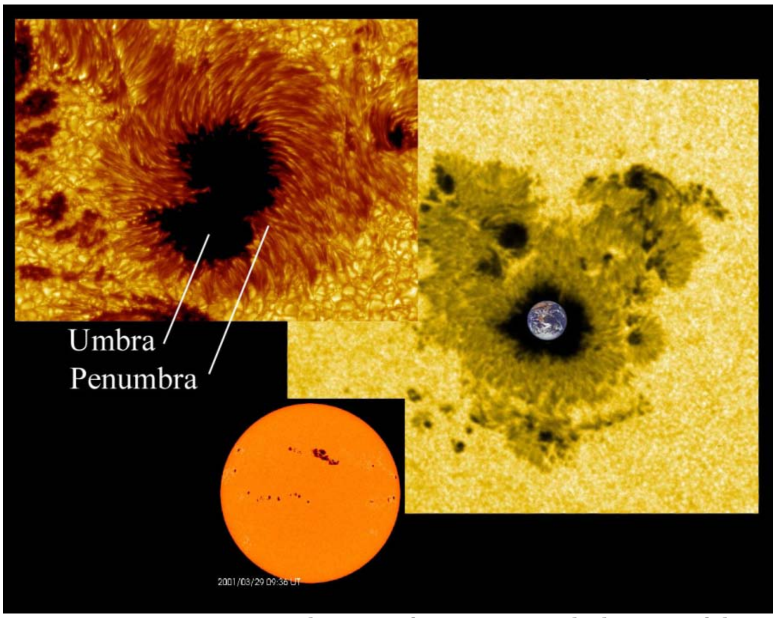

Fig. 1.3. Sunspot – comparing the size of a sunspot with the size of the earth
http://www.gsfc.nasa.gov/gsfc/spacesci/solarexp/sunspot.htm

The number of sunspots that appear on the 'solar disk' in a certain period of time is variable. There are periods of time when the number of sunspots rises quickly, while few years later, it falls more slowly on an irregular cycle. These periods are called sunspot maxima and sunspot minima, respectively. This periodic behavior in the sunspot population appearing on the sun is known as the sunspot cycle. The average length of time between two sunspot maxima or minima is about 11 years, and is called the 11-year cycle (figure 1.4).

The intense magnetic field in the sunspots prevents any convection in these regions and consequently the energy transport from the hot interior to the surface is reduced. On the other hand, this powerful magnetic field leads to strong heating in the solar atmosphere, forming active regions that are the source of intense solar flares and coronal mass ejections (CME).

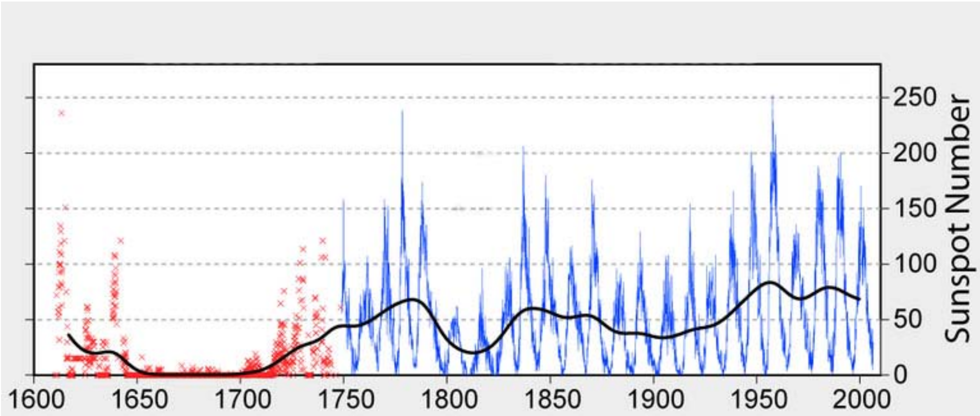

Fig. 1.4. 400 years of sunspot observation
Picture created by: Robert A. Rohde - Global Warming Art

The pairs of sunspots usually have opposite magnetic polarities. For a given sunspot cycle, the polarity of the leader spot (or leader spot-group) is always the same for a given hemisphere. At the beginning of a new cycle, the polarities reverse. This reveals that the full magnetic cycle is not the 11 years of the sunspot cycle but 22 years, known as the "Hale cycle". [1]

The period of least solar activity during which, the population of the sunspots diminishes, is known as solar minimum. On the other hand, the period of greatest solar activity during which, numerous numbers of sunspots appear on the photosphere is called the solar maximum.

1.4.2. Solar Irradiance Variations due to solar cycles

Taking into account the periodic appearance of the sunspots, it is logical to conclude that the sun luminosity must be affected by darkening of the sunspots.

At sunspot maximum, the total solar irradiance (TSI) is enhanced despite the presence of more dark spots, the reason is the increase in the number of small and bright faculae. Faculae are in a way the opposite of sunspots. Sunspots are darker than normal spots on the photosphere, while faculae are brighter than normal regions. As descused before, sunspots are areas where the sun's concentrated magnetic field *deflects* hot material flowing upward from the interior producing cooler regions. Faculae form where the magnetic field *concentrates* hot material flowing from the interior producing a hot spot. Faculae always form in areas surrounding sunspots.

Faculae are produced by small-scale photospheric magnetic flux tubes (radius below about 250 km) on the solar surface. The main difference between the faculae and sunspots is that their smaller radii allow radiation from the surrounding walls to maintain the temperature near 5770 K. The high magnetic pressure in the tube ($B^2/2\mu_o$) requires a lower particle pressure (Nk_BT) in equilibrium. Since the temperature is constant, the concentration N must be reduced, resulting to the increase of the optical depth, and this allows the observer to see deeper into the Sun, where the temperature is higher. As a result, the effect of the faculae is reverse to that of the sunspots, and so they look brighter than the surrounding photosphere, and giving an excess emission. [3]

The faculae are appearing and disappearing on the photosphere for up to 6 months. They give rise to the total solar irradiance by a factor of 0.05%. Their average temperature is 5920°K and they cover 3% of the solar hemisphere. On the other hand, the sunspots cover only 0.3% of the solar hemisphere and they appear on the photosphere no more than 100 days. Since the faculae are numerous and persist longer on the photosphere compare to the sunspot, the net effect during periods of enhanced magnetic activity of the sun is increasing radiant output of the sun. On average, the variation in solar luminosity in a complete 11 year solar cycle is about 0.1%. However the variation in UV region of the solar spectrum is as high as 100% (figure 1.5). [7]

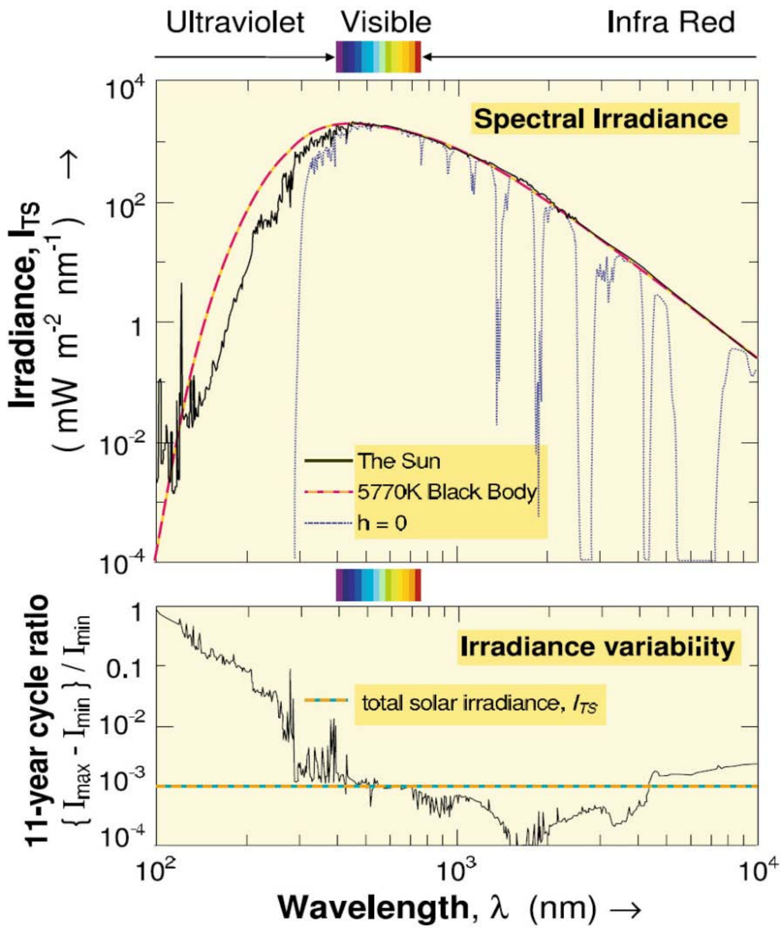

Fig. 1.5. Solar spectrum (top panel) and variations in solar irradiance due to 11 year solar cycle
From the book: The Sun, Solar Analogs and the Climate; I. Rühedi, M. Güdel and W. Schmutz

	Sunspots	Faculae
Surface Temp	3700-4100 K	5920 K
% of solar hemisphere	~ 0.3 %	~ 3 %
Radius	~ 10000 km	~ 100 km
Life time	< 100 days	~ 100 hours
Total time of appearance	< 100 days	~ 6 months
Effect on luminosity	< - 0.3 %	< + 0.05 %

Table 2. comparison between sunspots and faculae

1.5. Sun Atmosphere and Radiative Transfer

As mentioned in section 1.2. the region above the photosphere is called the solar atmosphere which is consist of tenuous and transparent gases. Normally the brilliance of the photosphere prevents us from seeing the thin solar atmosphere. The solar atmosphere is divided into two main regions, the chromosphere and the corona which are often rocked by enormous eruptions and explosion called prominences and flares.

1.5.1. Chromosphere

Chromosphere is a reddish layer of the solar atmosphere just above the photosphere. The thickness of this layer is approximately 4000 km. Its temperature increases from a minimum of about 4000 K to 6000 K. Above this altitude, the temperature rises drastically, reaching about 500,000K. The most common solar features within the chromosphere are spicules. Spicules are long thin fingers of luminous gas. They move upwards at the speed of about 20 km/s from the photosphere and live for about 5–10 minutes. [1]

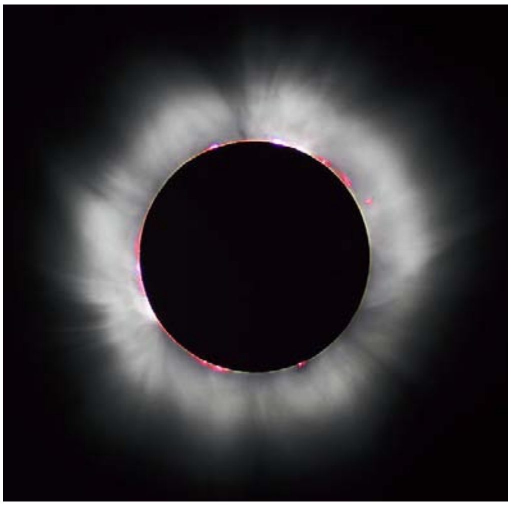

Fig. 1.6. The Chromosphere (reddish thin layer) and the Corona (white glowing cloud)
Photo by *Luc Viatour* - www.lucnix.be

1.5.2. Corona

Above the chromosphere lies the corona. The corona layer extends out millions of kilometers into the space forming the solar wind, which fills all the Solar System. It is visible as a faint white halo during total eclipses. It is generally believed that the corona has no outer boundary. The average temperature of the corona and solar wind is about 1 to 2 million K, however in some hottest regions it rises to 8 to 20 million K.

For more than 50 years Since the corona's temperature was first measured, it has been always a question for scientists why the temperature of the corona is three million K while the visible surface of the Sun is only about 6,000 K.

It is physically impossible to transfer thermal energy from the cooler photosphere to the much hotter corona. This incredibly hot temperature of corona requires a permanent heating mechanism, or the plasma in solar corona would cool down in about an hour.

According to recent research, solar physicists have identified small patches of magnetic field covering the entire surface of the Sun. These patches appear and disappear randomly in time scales of 40 hours. Scientists now think that this magnetic carpet is probably a source of the corona's heat. Based on the laws of electromagnetism, the intersection of two magnetic field lines of these patches is prohibited. Meaning that every time the magnetic field lines come close to cross each other, they are "rearranged", and this magnetic reconnection continuously heats the solar corona. This is just a theory and no magnetic reconnection has been observed yet. [6a]

1.5.3. Radiation in the Solar Atmosphere

The chromosphere consists of relatively cool gases lying over the hotter gases. These cool gases absorb the radiation from the photosphere at specific wavelengths which are characteristic of the atoms in the sun, and generate the solar absorption spectrum (figure 1.7).

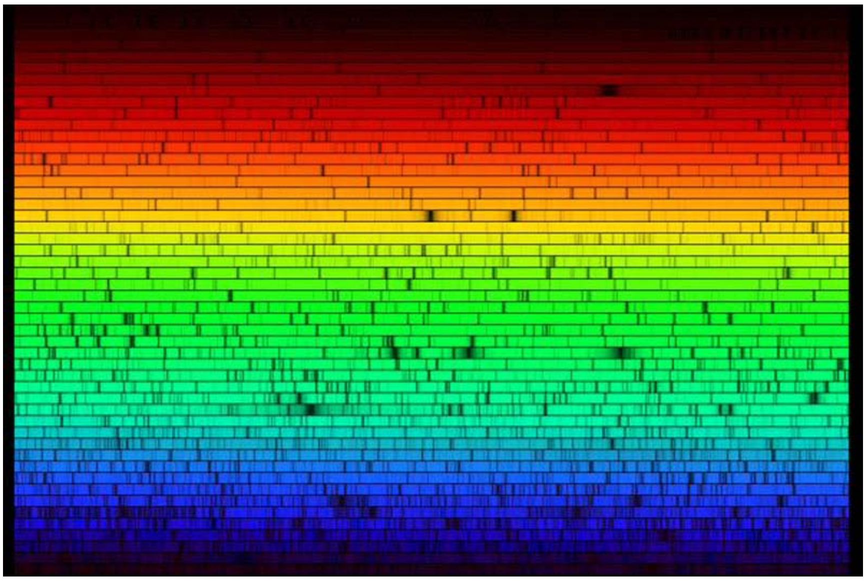

Fig. 1.7. Solar spectrum and Fraunhofer lines

Source: Nigel Sharp, National Optical Astronomical Observatories/National Solar Observatory at Kitt Peak/Association of Universities for Research in Astronomy, and the National Science Foundation. Image ID: High Resolution Solar Spectrum.

When the radiation encounters with matter, the energy of the radiated photons is transferred to the electrons of the atoms and push them to a higher energy state. The excited atoms then undergo a transition to a lower energy state and re-emit the energy. Electromagnetic radiation emerging from within the sun is continuously emitted and absorbed by atoms.

As shown in figure 1.8, the radiative temperature first drops to a minimum value of about 4500 K just above the photosphere, then slowly rises in the chromosphere and finally increased abruptly in the transition region to several million degrees in the corona. At each temperature, the probabilities of electronic transition in the atoms exist. This fact leads to the formation of absorption lines at different levels in the solar atmosphere.

The core of a line forms at the temperature in which there is a maximum transition probability for an electron to undergo a certain transition between two energy states. The wings of a line form at different temperature levels because of the required transition probabilities. Each absorption line has a preferred formation region in the solar atmosphere.

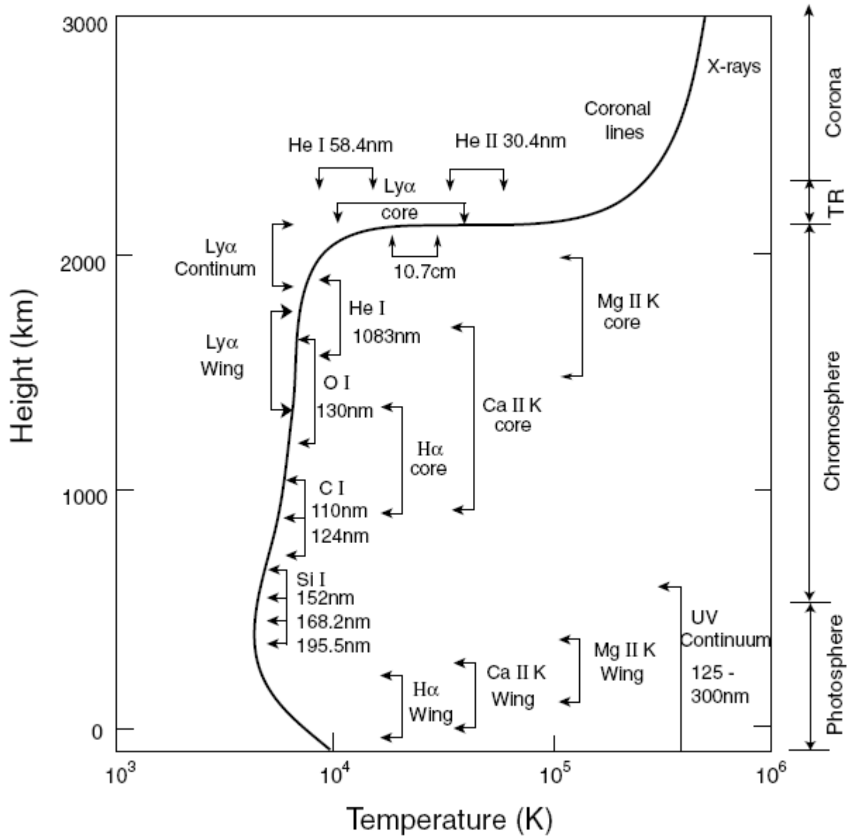

Fig. 1.8. The temperature structure of the solar atmosphere and the regions where absorption lines are formed. Data constructed from the results published in Lean (1987) and Livingston et al. (1988). The symbols I and II denote a neutral atom and a singly ionized atom, respectively, and TR refers to the transition region. [1]

The solar spectrum covers wavelengths from radio waves to gamma rays. Due to absorption, this spectrum is not completely continuous. The most important absorber in the sun is hydrogen, both in its neutral state and as negative ions. There are many other atoms in the sun that can absorb radiation. The first scientist who systematically studied the dark lines in the solar spectrum was German scientist, Joseph Fraunhofer (in 1814). He carefully measured the wavelength of the dark lines in optical spectrum. He mapped over 570 lines, and designated them with the letters A through K, and weaker lines with other letters.[9] due to Fraunhofer's work, the visible and near infrared and UV regions of the solar spectrum is known as the *Fraunhofer spectrum*. (figure 1.9, table 2) The strongest lines in Fraunhofer spectrum are produced by H, Mg, Fe, Ca, and Si and ionized Ca and Mg.

It is clear that the lines in the sun's emission spectrum are the same as those in its absorption spectrum (both produced by the same electronic transitions but in the reverse direction). When the photosphere is eclipsed, line emissions in the chromospheric spectrum, mostly from hydrogen, helium, and calcium, can be observed. The Hα line at 6563˚A is one of the strongest absorption lines in the solar spectrum. Normally the photospheric luminosity covers the large amount of energy emitted in this line in chromosphere, but at the beginning and end of a total eclipse and at the limb of the solar disk, the reddish color of this emission line is visible. [1]

The strong emission lines of hydrogen and helium originating in the chromosphere gradually fade out with increasing height and are replaced by the continuous spectrum of white light characteristic of the corona. There several weak emission lines in coronal spectra among which, the green line of ionized iron is the most intense one. The generation of such line requires a very large amount of energy. This was one of the first evidences that reviled the enormous temperature of the corona, which is in the order of 10^6K.

In general, the energy emitted by the Sun is divided into 40% visible light, 50% IR, 9% UV and 1% x-ray, radio, etc. The light we see is emitted from the ``surface'' of the Sun, the photosphere. The Sun below the photosphere is opaque and hidden.[10]

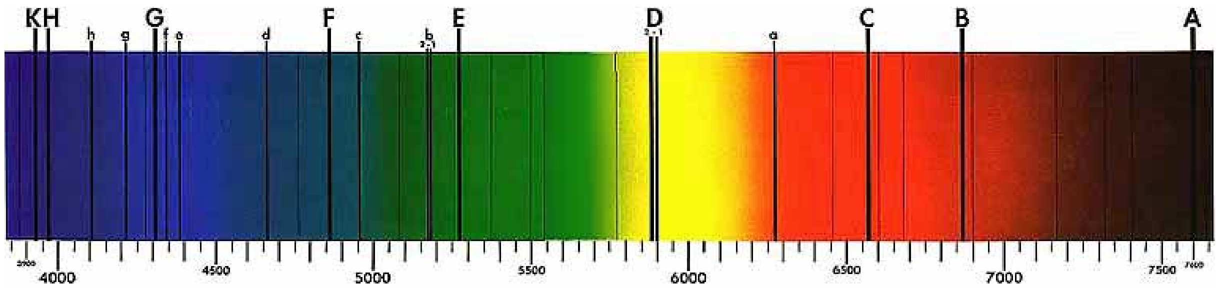

Fig. 1.9. Fraunhofer Spectrum
Source: European Southern Observatory - www.eso.org

Designation	Element	Wavelength (nm)	Designation	Element	Wavelength (nm)
y	O2	898.765	c	Fe	495.761
Z	O2	822.696	F	H β	486.134
A	O2	759.370	d	Fe	466.814
B	O2	686.719	e	Fe	438.355
C	H α	656.281	G'	H γ	434.047
a	O2	627.661	G	Fe	430.790
D1	Na	589.592	G	Ca	430.774
D2	Na	588.995	h	H δ	410.175
D3 (or d)	He	587.5618	H	Ca+	396.847
e	Hg	546.073	K	Ca+	393.368
E2	Fe	527.039	L	Fe	382.044
b1	Mg	518.362	N	Fe	358.121
b2	Mg	517.270	P	Ti+	336.112
b3	Fe	516.891	T	Fe	302.108
b4	Fe	516.751	t	Ni	299.444
b4	Mg	516.733			

Table 3. Fraunhofer major lines
Source: encyclopedia.stateuniversity.com

References:

1. K. N. Liou: ***An Introduction to Atmospheric Radiation (2nd Edition);*** *Elsevier Science (USA), 2002*

2. Heather Couper, Nigel Henbest**:** ***Space Encyclopedia;*** *DK Publishing, Inc., 2009*

3. I. Rühedi, M. Güdel and W. Schmutz: ***The Sun, Solar Analogs and the Climate (text book)****, Swiss Society for Astrophysics and Astronomy, 2004*

4. **Strobel's Astronomy Notes.** www.astronomynotes.com

5. ***Views of the Solar System web site***: copyrighted *by Calvin J. Hamilton. http://www.solarviews.com/eng/sun.htm*

6. ***NASA's Godard Space Flight Center****; http://solarscience.msfc.nasa.gov/SunspotCycle.shtml*

7. Willson, Richard C.; H.S. Hudson: ***The Sun's luminosity over a complete solar cycle****; Nature 351: 42–4. (1991)*

8. ***NASA's Godard Space Flight Center*** *http://imagine.gsfc.nasa.gov/docs/science/mysteries_l1/corona.html*

9. Jenkins, Francis A.; White, Harvey E.:, ***Fundamentals of Optics (4th ed.)****, McGraw-Hill, 1981*

10. Coulson, K. L.: ***Solar and Terrestrial Radiation***.; *Academic Press, New York. (1975)*

Chapter 2 : Magnesium

2.1. Physical Properties of Magnesium

Magnesium (Mg) is a chemical element with atomic number 12, oxidation number +2 and density of 1.738 g/ml. It is the eighth most abundant element in the Earth's crust by mass, and ninth in the Universe [1],[2]. Magnesium can be detected in all stellar atmospheres. This is because magnesium can easily built up in extra energetic conditions in supernova stars from three helium nuclei. The melting and boiling Points of magnesium are 923.15 K and 1380.15 K, respectively, meaning that it is not surprising to find this element in gaseous phase in different zones in the sun. The strongest absorption lines of magnesium in optical range are visible in figure 1.9. A Magnesium emission spectrum in visible range is illustrated in figure 2.1.

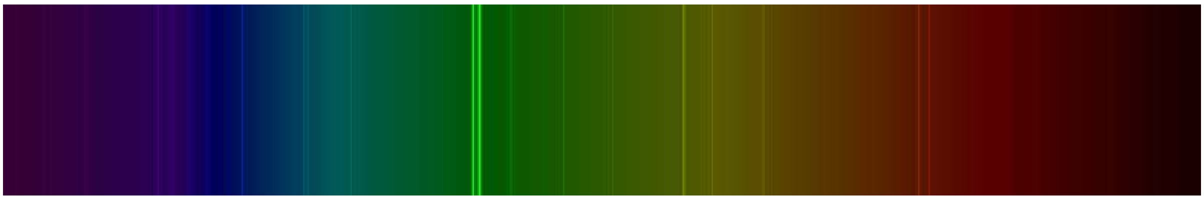

Fig. 2.1. Spectrum of Magnesium in visible region as emission lines in an electrical gas discharge. Note that a faint continuum was added only to give a better impression of the location of the colors in the spectrum. Source: National Institute of Standards and Technology.

The characteristic absorption (or emission) lines of Mg are not only in the visible region, but also in UV region of electromagnetic spectrum.

2.2. Ionized Magnesium Doublet (Mg II)

As seen in figure 1.9 and 2.1, some of the absorption lines in the spectrum appear in pairs, known as doublets. The individual lines in these doublets are marked by letters. As mentioned before this method of designating the lines was first introduced by Fraunhofer. In figure 1.9 the H and K doublet of ionized Calcium is clearly visible. By analogy with the Fraunhofer H and K lines for Ca^+ and to avoid confusion, authors use the notation *h* (280.27 nm) and *k* (279.55 nm) for so-called *Mg II* lines.[3] The Mg II energy diagram is illustrated in figure 2.2.

The reason that Magnesium has two adjacent emission lines at 280 nm is the especial electron configuration of the magnesium atom which is: $1s^2\ 2s^2p^6\ 3s^2$. By excitation, one electron jumps from 3s orbital state to 3p. Due to spin-orbit interaction (which basically is an electromagnetic interaction between the electron's spin and the nucleus's electric field, through which it moves), the energy level in 3p orbit is splitting into two adjacent energy levels. These fine structures can be deferred by a new set quantum numbers: The total angular momentum (j) and the projection of the total angular momentum (m_j), which the latter is a summation of the magnetic quantum number (m_l) and the spin projection quantum number (m_s). The two energy levels of 3p orbit are now differed by different values of m_j, which are equal to $\frac{1}{2}$ and $\frac{3}{2}$. This quantum number has only one value at 3s state: $m_j = \frac{1}{2}$. This means that transition from 3p to 3s has two probabilities: $3p_{3/2} \rightarrow 3s_{1/2}$ and $3p_{1/2} \rightarrow 3s_{1/2}$. Each of these return transitions produces an emission line at energy level approximately equal to 4.40ev with 0.01ev spacing between the two transitions, and this is the origin of the two emission lines for Magnesium at 280 nm. (This effect can be observed in emission spectrum of many elements and is known as *splitting of spectra lines*).

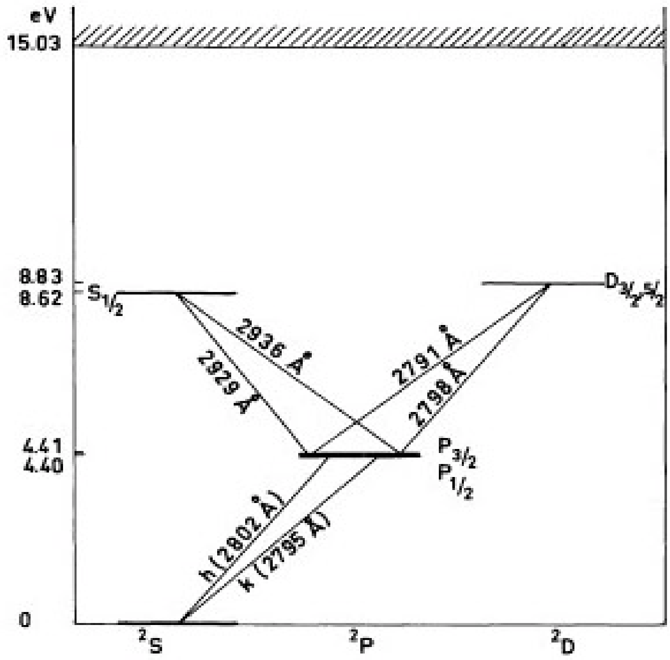

Fig. 2.2. MgII energy diagram [3]

2.3. Magnesium in Astronomy and Sun

One of the greatest achievements in the investigation of stellar atmospheric astronomy was the discovery of the resonance doublet Mg II of ionized magnesium (near 280 nm) in the spectra of stars of almost all spectral classes. The wide range of occurrence and the diversity of its forms make this doublet into one of the most powerful means for studying the physical nature of stars, nebulas, stellar atmospheres and the interstellar medium, etc [4].

The solar absorption doublet of magnesium was first discovered by Kachalov and Yakovleva in 1962, then studied theoretically by Dumont and separately by Athay and Skumanich in 1967[5],[3]. These studies among many others indicate a broad Mg II *absorption* feature in the UV spectrum of the sun which is centered at a wavelength of about 280 nm.

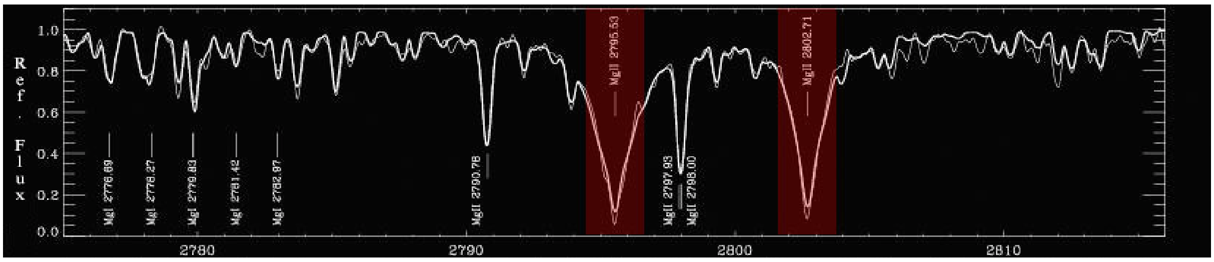

Fig. 2.3. Spectrum of the UV region around the resonance lines Mg I and Mg II in Vega, a bright standard star of the summer sky in the northern hemisphere.
Source: Dr. Karl Remeis-Sternwarte Bamberg -Astronomical Institute of the University Erlangen-Nürnberg

Although we expect two individual absorption lines for the Mg II doublet in the sun spectrum, like that of the star Vega (Comparing figures 2.3. and 2.4.), we can see only a single broad absorption feature. This is because the two Mg II absorption lines in the solar spectrum overlap. The source of this broad absorption line is the photosphere. By contrast, there are two Mg II emission lines located at the base of this composite feature originated in higher altitudes in the solar atmosphere, the chromosphere (figure 1.10). As explained in chapter 1, the absorption and emission lines occur for the same electronic transitions but in the opposite directions. The outgoing radiation from lower layers of the sun undergoes absorption in the photosphere as well as the solar atmosphere, on the other hand, the temperature variation in the chromosphere due to occurrence of faculae and CMEs (which are generated by eruption of magnetic field lines through the sunspots), leads to appearance of emission lines exactly at the center of the same absorption lines in the solar spectrum.

The broad absorption feature originated in photosphere shows much less variability, while the h and k emission lines are highly influenced by temperature variation in the chromosphere. At solar maximum, the number of sunspots on the photosphere increases. As a result the concentration of hot faculae in overlaying layer will be enhanced and the temperature of the chromosphere rises. Consequently the emission lines of Mg II in solar UV spectrum become stronger and more visible. (figure 2.4)

2.4. Mg II Index (core-to-wing ratio)

Basically, the Mg II index is the ratio of the irradiance at the core of the Mg II absorption feature, containing the variable emission lines originated in chromosphere, to that of its relatively less variable wings, which are generated in photosphere. Because the Mg II index is an irradiance ratio from proximate wavelength ranges, unwanted instrumental effects tend to cancel. As a result, the Mg II index is relatively uncorrupted by such instrumental effects.

The Mg II emission lines contain information on the temperature fluctuations that occur in the chromosphere. During the solar maxima, the temperature of the chromosphere is increasing and more molecules of magnesium getting excited. Consequently the emission lines (or core) become more intense, while the wings of the absorption feature retain their shapes. Hence, the core-to-wing ratio or the so-called Mg II Index will be increased in magnitude. On the other hand, when temperature of the chromosphere drops in periods of solar minima, the emission lines become weaker and the magnitude of the index decreases.

For this reason, the Mg II index has widely been used to estimate the contribution of faculae to Total Solar Irradiance (TSI) especially in the ultra violet region. This method was originally described by Heath and Schlesinger in 1986 and Donnelly in 1988.

The procedure which has been used to produce the Mg II index in this study will be explained in chapter 5.

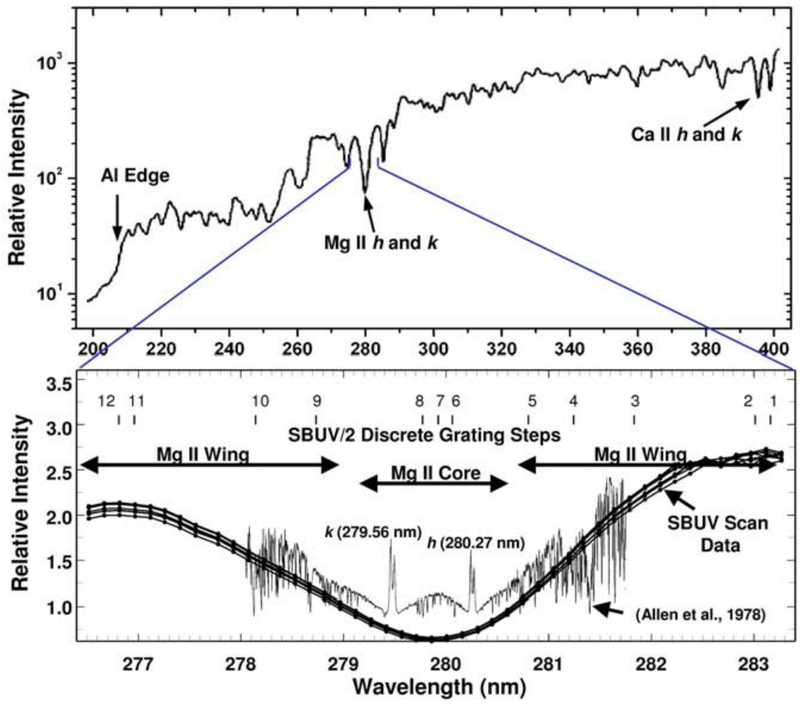

Fig. 2.4. (top) Solar UV spectrum illustrating the absorption pattern and (bottom) details of the UV spectrum around the Mg II spectral feature at 280 nm, where emission lines appear with higher resolution [6].

References:

1. Housecroft, Catherine E; Sharpe, Alan G.: ***Group 2 metals;*** *Inorganic Chemistry (3 ed.). Harlow, England, 2007*

2. Ash, Russell: ***The Top 10 of Everything 2006: The Ultimate Book of Lists***

3. Lemaire, P. & Skumanich, A.: ***Magnesium II Doublet Profiles of Chromospheric Inhomogeneities at the Center of the Solar Disk;*** *Astronomy and Astrophysics, Vol. 22, p. 61 (1973)*

4. V. G. Cholakyan: ***Intensities of the resonance lines of neutral and ionized magnesium in stellar spectra;*** *Astrophysics, Vol. 25, No.2 (1986)*

5. B. Bates, D. J. Bradley, D. A. McBride, C. D. McKeith, N. E. McKeith, W. M. Burton, H. J. B. Paxton, D. B. Shenton and R. Wilson: ***High Resolution Interferometric Studies of the Solar Magnesium II Doublet Spectral Region;*** *Philosophical Transactions of the Royal Society of London. Series A, Mathematical and Physical Sciences, Vol. 270, No. 1202, A Discussion on Solar Studies with Special Reference to Space Observations (Jul. 16, 1971), pp. 47-53*

6. Rodney A. Viereck, Linton E. Floyd, Patrick C. Crane, Thomas N. Woods, Barry G. Knapp, Gary Rottman, Mark Weber, Lawrence C. Puga, and Matthew T. DeLand: ***A composite Mg II index spanning from 1978 to 2003;*** *Space Weather, vol. 2, 2004*

7. Swiss Society for Astrophysics and Astronomy, edited by I. Rühedi, M. Güdel and W. Schmutz: ***The Sun, Solar Analogs and the Climate*** *(text book), 2004*

8. The Naval Research Laboratory Solar Physics Branch, http://wwwsolar.nrl.navy.mil/

9. Donnelly, R. F., L. C. Puga, J. Barrett, S. D. Bouwer, J. Pap, D. E. Stevens, and W. K. Tobiska (1994): ***Solar UV flux measurements from the SBUV2 monitor on the NOAA-9 satellite: Part 1. Mg II hand k line core-to-wing ratios for 1986 – 198;,*** *NOAA Tech. Memo. ERL SEL-85, 211 pp., Natl. Oceanic and Atmos. Admin., Boulder, Colorado*

10. Heath, D. F., and B. M. Schlesinger: ***The Mg 280 nm doublet as a monitor of changes in the solar ultraviolet irradiance****, J. Geophys Res., 91, 8672-- 8682. (1986)*

Chapter 3 : Instrumentation

3.1. SCIAMACHY instrument

SCIAMACHY (Scanning Imaging Absorption Spectrometer for Atmospheric CHartographY) is an imaging spectrometer which was launched on March 1, 2002 onboard the European Environmental Satellite (Envisat-1) from Kourou, French Guiana. The primary mission objective of this instrument is to perform global measurements of trace gases in the Earth's atmosphere. SCIAMACHY was the first satellite instrument to observe daily solar spectral irradiance (SSI) continuously from 230 nm (UV) to 1750 nm (near-IR) [1]. The SCIAMACHY instrument was proposed in 1988 by the SCIAMACHY team [*Burrows et al., 1988*] and is jointly funded by Germany, The Netherlands and Belgium.

The Envisat satellite operates in a near-polar sun-synchronous orbit. The mean altitude of the satellite is 799.8 km and the angle of inclination of its orbit is 98.55° with a period of 100.6 min (about 14.6 orbits per day). The satellite rotates the earth with an orbital velocity of approximately 7.45 km/s over ground crossing the equator on the descending node at about 10:00 local time. The inclination angle of 98° means that the satellite moves slightly against the rotation of the Earth and passes close to the poles, having a repeated orbital cycle of 35 days (501 orbits) [2],[3]. The SCIAMACHY instrument is a UV, visible and shortwave infrared, passive and moderate-resolution imaging remote sensing spectrometer. The spectral information is observed in 8 channels covering a wide spectral range from 214-2386 nm and has a spectral resolution between 0.24 nm and 1.48 nm (Table 3.1) [2].

Channel	Range (nm)	Resolution (nm)	Stability (nm)	Temp. Range (K)
1	214 - 334	0.24	0.003	204.5 – 210.5
2	300 - 412	0.26	0.003	204.5 – 210.5
3	383 - 628	0.44	0.004	221.8 – 227.8
4	595 - 812	0.48	0.005	222.9 – 224.3
5	773 - 1063	0.54	0.005	221.4 – 222.4
6	971 - 1773	1.48	0.003	197.0 – 203.8
7	1934 - 2044	0.22	0.015	145.9 – 155.9
8	2259 - 2386	0.26	0.003	143.5 – 150.0

Table. 3.1. SCIAMACHY channels (1 & 2 = UV, 3 & 4 = VIS, 5 = NIR, 6-8 = SWIR)
Source: SCHIAMACHY, Monitoring the Changing Earth's Atmosphere (text book, p.37)

SCIAMACHY observes the atmosphere in three different viewing geometries: Nadir, Limb and Occultation (figure 3.1):

- **Nadir:** In this geometry, the instrument looks downward in order to record the scattered solar radiation in the atmosphere or reflected radiation from the surface, from underneath the satellite.

- **Limb**: In the limb viewing geometry, the observing line of the instrument is tangential to the Earth's surface, starting at about 3 km below the horizon and then scanning vertically up to the top of the atmosphere (about 100 km tangent height).

- **Occultation:** In this mode, the instrument tracks the sun or moon during its rise behind the earth, thus recording transmitted solar radiation for different tangent altitudes.

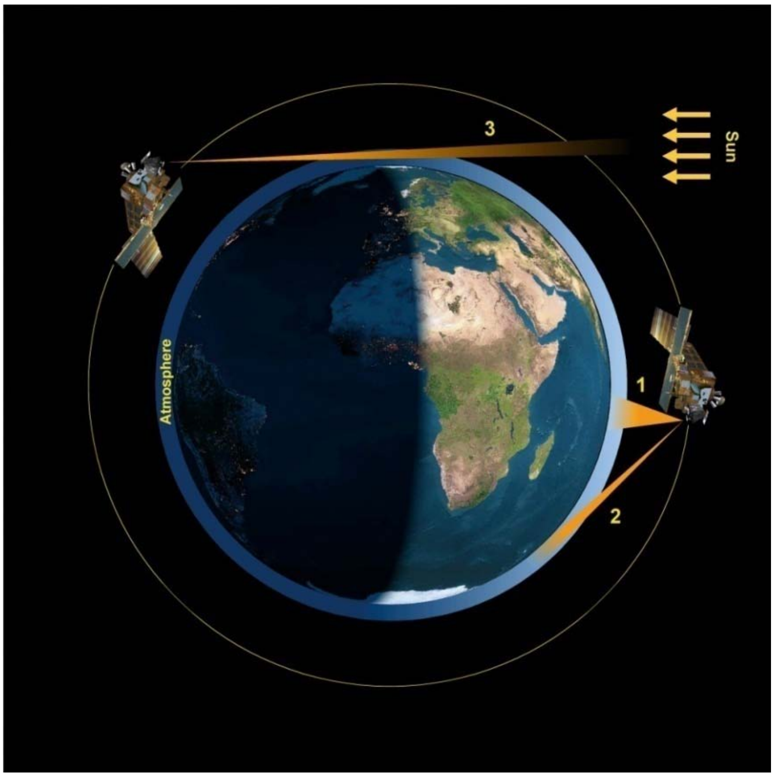

Fig. 3.1. Observation geometries of SCIAMACHY. Nadir (1), Limb (2), and Occultation (3)
Source: SCHIAMACY, Monitoring the Changing Earth's Atmosphere (text book, p.45)

3.1.1. Sun Observations by SCIAMACHY

At the local time 10 a.m. during descending node crossing, the sun is always to the left of the flight direction, meaning that the azimuth angle is bigger than 180°. The maximum solar elevation is about 70° [2]. Sunrise occurs after ascending node crossing when the satellite moves towards the North Pole on the eclipse side of the orbit (figure 3.2). Once the sun has risen, it is tracked by the ESM for the complete pass through the SO&C (Sun occultation & calibration) window. The "start of calibration & monitoring measurements above atmosphere" event starts when the sun reaches the altitude of 150 km [5].

For each viewing geometry different combinations of scan mirrors (elevation and azimuth scan mirrors) and diffusers (mounted on the back of each scan mirror) are used to observe the sun [1],[2]: In limb-occultation geometry via ASM and ESM mirrors, in nadir geometry via the ESM mirror through the subsolar port, and via the so-called calibration light path involving the ASM mirror and the ESM diffuser[4] (the mirrors and the diffusers are illustrated in figure 3.3).

The light path which provides solar spectral irradiance in physical units from the full solar must be radiometrically calibrated. The only path that satisfies this condition the one involves the Azimuth Scan Mirror (ASM) and the diffuser mounted on the back of the Elevation Scan Mirror (ESM diffuser). The diffuser scatters solar light into a diffuse beam to illuminate the entrance slits evenly [1].

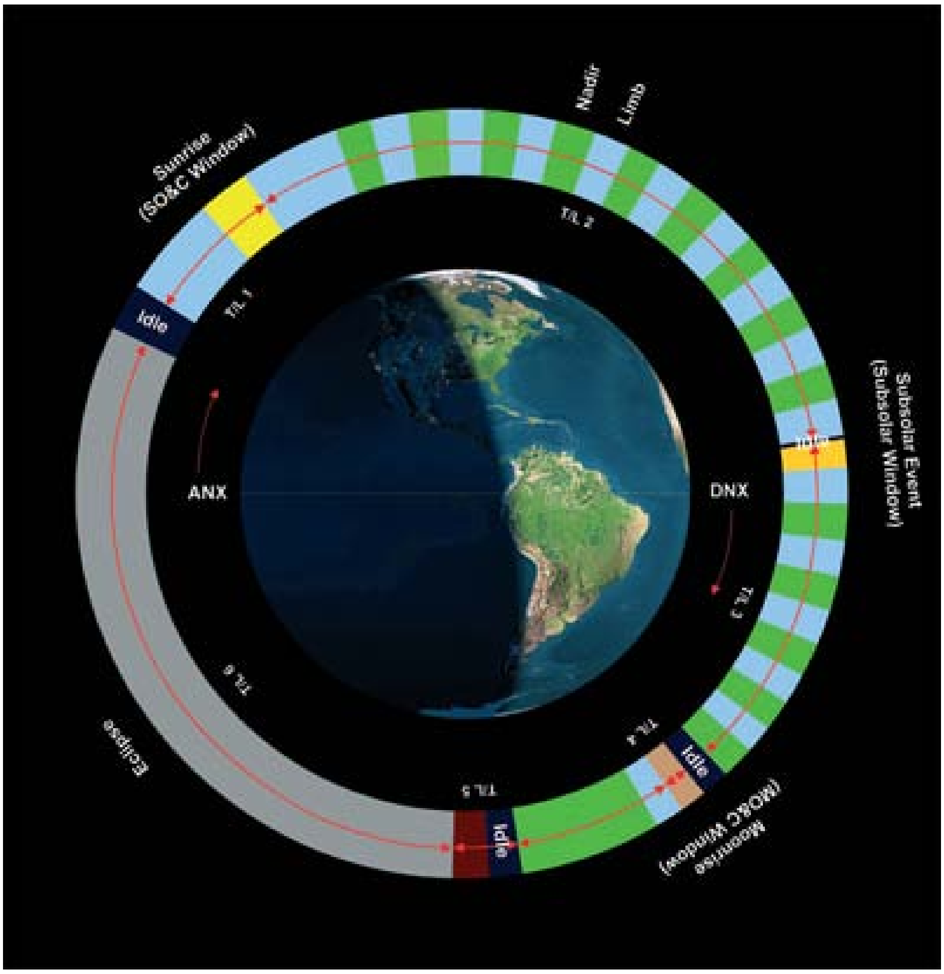

Fig. 3.2. SCIAMACHY reference orbit with sun/moon fixed events along the orbit. The events define orbital segments which are filled with timelines [2].

The incoming light is pre-dispersed by a prism and dispersed by holographic diffraction gratings in each of the eight channels of the instrument. For the five short wavelength channels (up to 1063 nm), EG&G Reticon diode arrays with 1024 detector pixels are used.

ESM diffuser solar measurements are carried out in most cases once a day. A measurement sequence lasts about 50 s from which a mean solar spectrum is derive. About 98% of the TSI (total solar irradiance) is covered by SCIAMACHY [1].

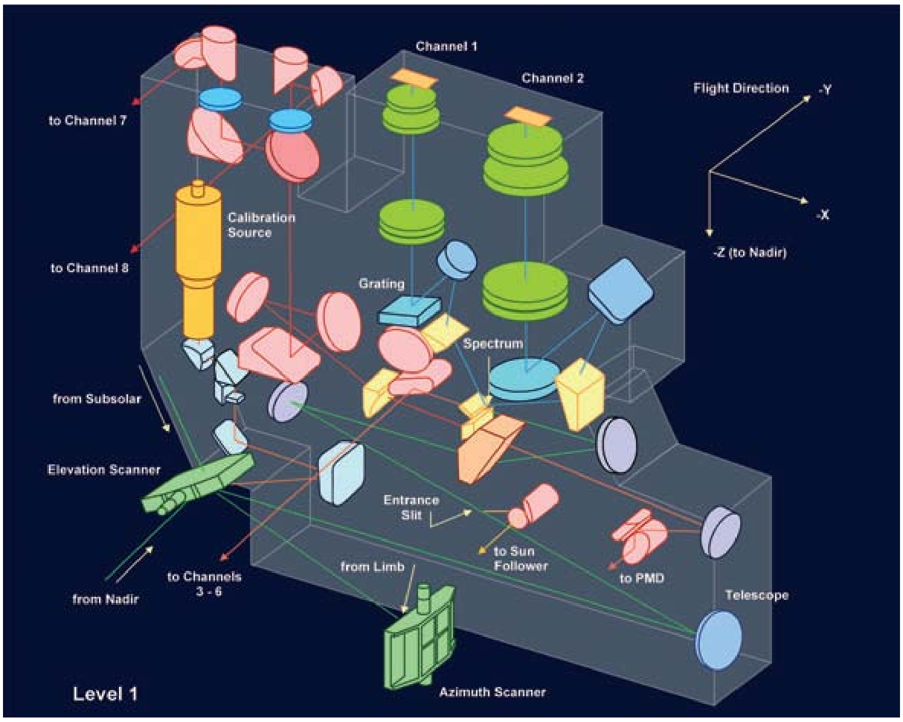

Fig. 3.3. Optical configuration of the mirrors and the diffusers in SCIAMACHY [2].

3.2. GOME instrument

GOME (The Global Ozone Monitoring Experiment) is the first European passive remote sensing instrument operating in the ultraviolet, visible, and near infrared wavelength regions. It was launched by ESA aboard the second European Research satellite (ERS-2) on April 21st 1995 [6].

Similar to ENVISAT-1 (the satellite board for SCIAMACHY), ERS-2 flies also in a sun-synchronous polar orbit with an inclination of 98° at an altitude of 780 km. This results in an orbital period of about 100 minutes and a speed of the sub-satellite point of 7 km/s and 14 orbits per day. The satellite crosses the equator at a local time of 10:30, flying from North to South [9].

Unlike SCIAMACHY the GOME instrument only performs – apart from the solar irradiance measurements – atmospheric measurements in nadir geometry. The maximum scan width in the nadir viewing is 960 km and global coverage is achieved within three days (after 43 Orbits). The scanning swath is divided in four ground pixels (named east, centre or nadir, west and backscan, with 1.5 sec integration time each. The scan measures 40 km in the direction of flight [8],[9]. The scanning width and the orbit specification combined means that GOME obtains global coverage in 3 days (figure 3.3).

The primary mission objective of GOME is the monitoring of vertical columns of relevant atmospheric trace gases, such as O_3, $N0_2$, BrO, OCIO, $S0_2$, H_2CO, from the backscattered radiance and direct solar irradiance measurements [7].

Technically, GOME comprises entrance optics, a spectrometer, electronics and thermal systems. The main part, spectrometer, is basically a double monochromator which combines a predisperser prism and a holographic grating in each of the four optical channels as dispersing elements [8]. All spectrometer parts are fixed, except the scan mirror at the nadir view port. The spectra from 240 nm to 790 nm are recorded simultaneously. The spectral resolution varies between 0.2 nm (UV, Channel 1) and 0.4 nm (VIS, channel 4). (Table 3.2)

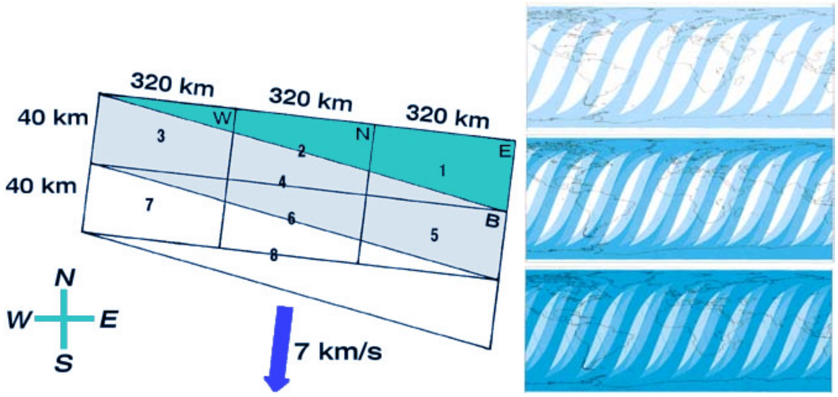

Fig. 3.3. left: GOME Scan Geometry in Nadir Viewing. Two successive scan sequences are shown. Forward scan consists of East (E), Nadir (N), and West (W) pixels and is followed by a backscan (B) [9]. right: the global coverage [10]

Channel Spectral	Range (nm)	Resolution (nm)	Integration time (sec)
1A	237-283	0.20	12
1B	283-316	0.20	1.5
2	311-405	0.17	1.5
3	405-611	0.39	1.5
4	595-793	0.33	1.5

Table. 3.2. GOME channels (1 & 2 = UV, 3 & 4 = VIS, 5 = NIR, 6-8 = SWIR) (Burrows et al. 1999 and GOMEMANUAL 1995) [9]

3.2.1. Sun Observations by GOME

GOME can record solar irradiance directly by observing the sun once a day (every 14th orbit) when the ERS-2 satellite crosses the terminator in the north polar region coming from the night side. GOME is not capable of actively tracking the sun. The full solar disk is visible to the instrument only for a time span of about 50 s. Integration times are 0.75 s for all channels, except for the UV channel, where the integration time is doubled. A mean solar spectrum is then produced from the series of measurements during the solar viewing period [6].

3.3. Comparison between SCIAMACHY and GOME

GOME is a small scale version of SCIAMACHY observing the atmosphere in nadir viewing geometry and having only four spectral channels, as opposed to eight channels for SCIAMACHY [8]. With such a wide wavelength coverage and relatively high spectral resolution and also applying various observing geometries, SCIAMACHY seems to be a more powerful instrument than GOME, in general. Regarding solar irradiance measurements, SCIAMACHY is capable of tracking the sun once every orbit and a mean solar spectrum is produced from the series of daily measurements. GOME can only observe the sun once a day. The integration time during which the solar disk becomes completely visible to SCIAMACHY is longer than that of GOME. Table 3.3 gives a brief comparison between the SCIAMACHY and GOME instruments.

	SCIAMACHY		GOME	
Type	Atmospheric Chemistry		Atmospheric chemistry	
Technical Characteristics	Spatial Resolution	Limb vertical 4 x 132km, Nadir horizontal 32 x 215km	Spatial Resolution	Vertical: 7-10 km (for O3), Horizontal: 40 x 40 km to 40 x 320 km
	Swath Width	Limb and nadir mode: 1000km (max)	Swath Width	120-960km
	Waveband	UV-SWIR: 240-314, 309-3405, 394-620, 604-805, 785-1050, 1000-1750, 1940-2040 and 2265-2380nm	Waveband	UV-NIR: 0.24-0.79µm (resolution 0.2-0.4nm)
Applications	Agriculture (Forest Fires) Atmosphere, Air Quality (Ozone), Atmospheric chemistry (Trace Gases) Atmospheric Temperature, Atmospheric Radiation, Clouds Solid Earth (Volcanoes), Oceans and Coasts (Ocean Color/Biology)		Atmosphere, Air Quality (Ozone), Atmospheric chemistry (Trace Gases), Clouds	
Solar observation				
full solar disk visibility	21 sec		50 sec	
Integration time	3.5 sec		1.5 sec (for UV channel)	

Table. 3.3. A comparison between SCIAMACHY and GOME [10]

3.4. SBUV instrument

The Solar Backscatter Ultraviolet Radiometer (SBUV), is an operational remote sensor which flies on the on the National Oceanic and Atmospheric Administration (NOAA) weather satellites. A family of eight SBUV sensors has been produced by Ball Aerospace & Technologies Corp. under contract to NASA/Goddard Space Flight Center and NOAA since 1978. Successive generations of the sensor have flown on Nimbus-7 (November, 1978 through June 21, 1999), NOAA 9 (December 1984 through August, 1993), NOAA 11 (September, 1988 through March, 1995), and NOAA 14 (December, 1994 through

September 21, 2000). NOAA 14 is replaced by NOAA 16 (September 21, 2000 through present). NOAA 17 launched June 2002 and NOAA 18 launched May, 2005.

The purpose of the SBUV instrument is to measure the solar irradiance and Earth radiance in the near ultraviolet spectrum (160 to 400 nm). From these data, the following atmospheric properties can be deduced [11]:

- The global and vertical distribution of stratospheric ozone
- The structure and dynamics of stratospheric ozone
- Photochemical processes and the influence of trace constituents on the ozone layer
- Long-term solar activity in the Ultraviolet spectrum

3.4.1. The Nimbus 7 and NOAA Platforms

Nimbus 7 was orbiting the Earth at the altitude of 955 km in a sun-synchronous polar orbit. The global coverage was achieved every six days (83 orbits). Because of power limitations aboard the spacecraft, sensors were not run simultaneously, but were scheduled on a priority basis. The Nimbus-7 platform allowed a number of experiments related to pollution control, oceanography, meteorology and solar irradiance monitoring to be conducted. Mission objectives were.

The NOAA-POES (NOAA-Polar Orbiting Satellites) series are named simply NOAA-9 through NOAA-17 in order of launch. The POES satellite system offers the advantage of daily global coverage, by making nearly polar orbits roughly 14.1 times per day. All NOAA-POES satellites have a circular, sun-synchronous polar orbit with a nominal flight height of 833 km. The even numbered satellites cross the equator at local solar times of approximately 7:30 and 19:30, while the odd-numbered satellites cross the equator at local solar times of approximately 2:30 and 14:30 [12].

3.4.2. Technical Properties

SBUV is a nadir pointing non-scanning instrument sensitive to radiation in near ultraviolet spectrum from 160 to 400 nm. The overall radiometric resolution is approximately 1 nm.

The most important parts of SBUV instrument are Two optical radiometers: a monochromator and a small but very important Cloud Cover Radiometer (CCR). The instrument contains four mechanisms: a movable grating for wavelength selection in the monochromator, a deployable diffuser which selects solar or Earth radiation measurements, a deployable Mercury lamp for wavelength calibration and an optical chopper mechanism which converts the steady incoming radiation to pulses of ultraviolet (UV) light which can be readily processed by the SBUV detectors and electronics. The use of a deployable diffuser gives the instrument the capability of selecting between solar and Earth measurements. With the diffuser "stowed", the instrument views the Earth directly. The data from this configuration corresponds to Earth radiance. With the diffuser deployed into the "Sun" position, the detector measures the solar irradiation. Ground and in-flight calibration data are used to convert the detector data and diffuser mode data to solar irradiation or Earth radiance units [13].

The NOAA SBUV Mg II measurement is one of the best chromospheric time series available for describing solar irradiance variations from daily to solar cycle timescales. Continuous daily values are available from 1978, covering three solar cycles. The SBUV measurements have been widely used in this work, especially for time period between 1978 and 1995, either as the reference measurements in final Mg II composite time series or for validation of the measurements from other instruments. For the time period after 1995, the GOME and SCIAMACHY have been assumed as the reference instruments. The details regarding the extraction and manipulation of the data from these instruments will be provided in chapter 5.

References:

1. J. Pagaran, M. Weber, and J. Burrows: ***SOLAR VARIABILITY FROM 240 TO 1750 nm IN TERMS OF FACULAE BRIGHTENING AND SUNSPOT DARKENING FROM SCIAMACHY****; The Astrophysical Journal, 700:1884–1895, August 2009*

2. M. Gottwald, H. Bovensmann, G. Lichtenberg, S. Noel, A. von Bargen, S. Slijkhuis, A. Piters, R. Hoogeveen, C. von Savigny, M. Buchwitz, A. Kokhanovsky, A. Richter, A. Rozanov, T. Holzer-Popp, K. Bamstedt, J.-C. Lambert, J. Skupin, F. Wittrock, H. Schrijver, J.P. Burrows: ***SCIAMACHY, Monitoring the Changing Earth's Atmosphere***; *Published by DLR, 2006*

3. von Savigny, C., A. Rozanov, H. Bovensmann, K. U. Eichmann, S. Nöel, V. V. Rozanov, B. M. Sinnhuber, M. Weber, J. P. Burrows, and J. W. Kaiser: ***The ozone hole break-up in September 2002 as seen by SCIAMACHY on ENVISAT****; J. Atm. Sci., 62, 721-734, 2005b*.

4. Stefan Noel, IFE/IUP: *http://www.iup.physik.uni-bremen.de/sciamachy/LTM/LTM.html*

5. SCIAMACHY Orbit Analysis , DLR: http://atmos.caf.dlr.de/projects/scops/orbit_analysis/orbit_analysis_actual.html#SO&C

6. Mark Weber: ***Solar Activity during Solar Cycle 23 monitored by GOME****: European Symposium on Atmospheric Measurements from Space, Proc. ESAMS'99, ESA-WPP-161, 325-332, 1999*

7. A. Menkhaus, M. Weber, C. Haite, J. P. Burrows: **Surface UV Modelling and Validation Using GOME Data;** *European Symposium on Atmospheric Measurements from Space, Proc. ESAMS'99, ESA-WPP-161, 325-332, 1999*

8. Institue for Environmental Physics (IUP), GOME Webpage: *www.iup.uni-bremen.de/gome/*

9. The Royal Netherlands Meteorological Institute, webpage: *www.knmi.nl/gome_fd/doc/gomeintro.html*

10. European Space Agency (ESA): *www.esa.int/esaCP/index.html*

11. The world data center for remote sensing of the atmosphere, DLR: *http://wdc.dlr.de/sensors/sbuv/*

12. NOAA Polar Orbiter Data User's Guide, Section 1.2, Orbital Information *www.ncdc.noaa.gov/oa/pod-guide/ncdc/docd/podug/htmal/c1/sec1-2.htm*

13. Goddard Space Flight center, NASA: *http://goespoes.gsfc.nasa.gov/poes/instruments/sbuv.html*

Chapter 4 : Wavelet Analysis

The most commonly used methods to analyze quasi-periodic signals are Fourier and wavelet analysis. The Fourier transform only provides information on the dominant frequencies, while wavelet analysis has a significant advantage compared to Fourier analysis; it can provide the time localization of the various frequency components. Because of this capability, wavelet analysis has been becoming a common tool for analyzing localized variations of power within a time series.

Basically, using wavelet transform one can decompose a time series into time–frequency space, and so it will be possible to determine the dominant modes of variability and the time variations of these modes [1]. In this sense, wavelet analysis is ideal for analyzing non-stationary time series or time series where one *expects localized variations of power.* This analyzing method is used in many fields of physics that involve the study of time series.

4.1. From Fourier to Wavelet transform

Wavelet Transform (WT) is a generalized form of Fourier Transform (FT) and Windowed Fourier Transform (WFT). The Fourier transform uses infinite sine and cosine base functions, so the FT of a stationary time series with a pure sine wave, will be a line spectrum (figure 4.1 a). The FT of a time series does not contain any information about the time dependency of the signal.

In a WFT, the time series is studied under a fixed time-frequency window with constant intervals in both domains. When a wide range of frequencies is involved, the fixed time window of WFT tends to contain a large number of high frequency cycles and a few low-frequency cycles. This results in an overrepresentation of high-frequency components and underrepresentation of the low-frequency components. Because of the constant frequency increment, the WFT does not have adequate resolution in the very low frequency band (figure 1.1 b).

A WT uses local base functions that can be translated with a flexible resolution in both frequency and time domain. Because of the "Uncertainty Principle", the width and height of a time-frequency window cannot be arbitrary chosen. As a result, high precision in time localization in the high-frequency band can only be achieved at the expense of reduced frequency resolution, and vice versa for low-frequency components (figure 1.1 c). In this way, a WT allows the wavelets to be scaled to match most of the low- and high-frequency signals in time, such as abrupt changes [2].

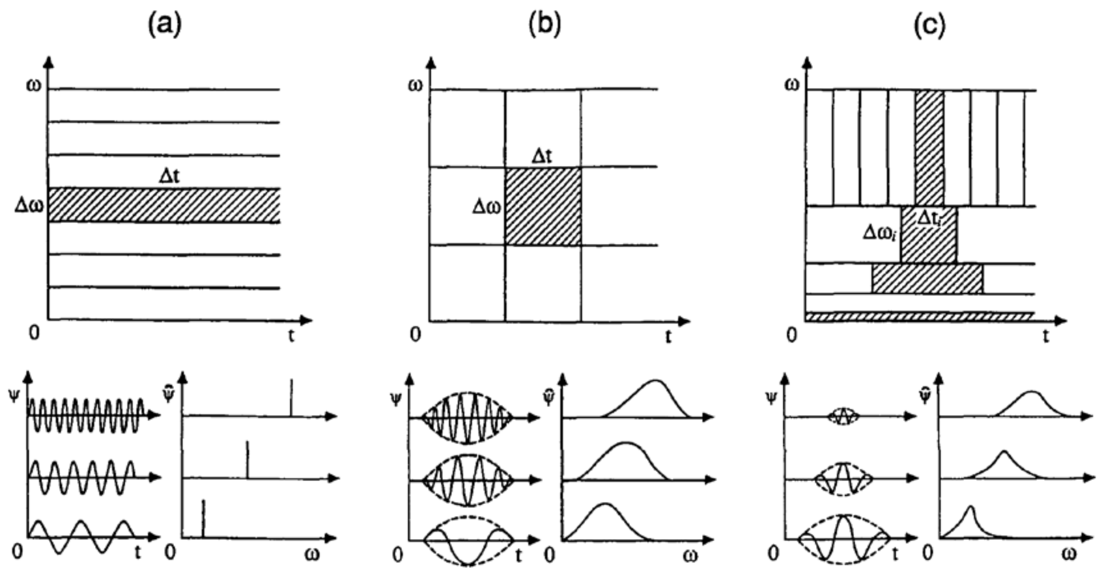

Fig. 1.1. Time frequency windows used in: (a) Fourier Transform (FT), (b) a Windowed Fourier Transform (WFT), and (c) a Wavelet Transform (WT), and their corresponding time series represented in time space and frequency space [2].

4.2. Wavelet Transform

The wavelet transform of a given function $f(t)$ (or a given time series x_n in discrete form) is defined as the convolution of $f(t)$ with an analyzing function $\psi(\eta)$. This analyzing function makes the basis of the time-frequency space into which the given function or time series is going to be decomposed. To be called a *wavelet*, the analyzing function must be localized both in time and frequency space and should be admissible, which, for an integrable function, means that its average should be zero. It is also assumed that ψ satisfies the normalization condition.

Normalization condition: $\int_{-\infty}^{+\infty} \psi^2(\eta)\, d\eta = 1$

Admissibility *condition:* $\int_{-\infty}^{+\infty} \psi\,(\eta) d\eta = 0$

For $\eta = (t' - t)/s$, the continuous wavelet transform is given by:

$$W(t,s) = \int_{-\infty}^{+\infty} f(t') \frac{1}{\sqrt{s}} \psi^* \left[\frac{(t'-t)}{s}\right] dt' \qquad eq.1$$

in which t is time, s is the wavelet scale and ψ^* is the complex conjugate. The factor $\frac{1}{\sqrt{s}}$ is necessary to satisfy the normalization condition,

$$s = \int_{-\infty}^{+\infty} \psi \left[\frac{(t'-t)}{s}\right] \psi^* \left[\frac{(t'-t)}{s}\right] dt' \qquad eq.2$$

In case of a discrete time series, x_n, of N observations with a time-step of δt, the integral in Equation *1* is replaced by a summation over the N time-steps. Hence, the continuous wavelet transform of a discrete time series is given by,

$$W(s) = \sum_{n'=0}^{N-1} x_{n'} \sqrt{\frac{\delta}{\sqrt{s}}} \psi^* \left[\frac{(n' - n)\delta t}{s} \right] \qquad eq.3$$

where s is again the wavelet scale and n provides the time variation (meaning that the term $n\delta t$ gives the total time of the time-series). The wavelet transform is built up by varying s and n, ensuring that the frequency components and their corresponding time localization are present.

To calculate the continuous wavelet transform of the time series x_n , the convolution ($eq.3$) should be done N times for each scale, where N is the number of data points in the time series (The choice of doing all N convolutions is arbitrary) [3]. According to convolution theorem, it is possible to do all N convolutions simultaneously in Fourier space using a discrete Fourier transform (DFT).

$$DFT(x_n) = \hat{x}_k = \frac{1}{N} \sum_{n'=0}^{N-1} x_n \, e^{-2\pi i k n/N} \qquad k = 0, \dots, N-1 \qquad eq.4$$

By the convolution theorem, the wavelet transform is the inverse Fourier transform of the product:

$$W_n(s) = \sum_{n'=0}^{N-1} \hat{x}_k \, \hat{\psi}^*(s\omega_k) e^{i\omega_k n\delta t} \quad \text{where} \quad \hat{\psi}(s\omega_k) = FT[\psi(t/s)] \qquad eq.5$$

The angular frequency ω_k now is defined as:

$$\omega_k = \begin{cases} \frac{2\pi k}{N\delta t}, & k \leq \frac{N}{2} \\ -\frac{2\pi k}{N\delta t}, & k > \frac{N}{2} \end{cases} \qquad eq.6$$

Having equation *5*, one can simply calculate the continuous wavelet transform for a given s at all n simultaneously. However, as the Fourier transform assumes the data is cyclic, and most time series are of finite length, this introduces errors at the edges of the transform. The region in which the transform suffers from these edge effects is known as the cone of influence (COI) [1]. The COI is defined so that the wavelet power for a discontinuity at the edges decreases by a factor e^{-2}. These discontinuities are introduced due to zero-padding at the beginning and the end of the time-series for each scale in order to bring the total length of the time-series, *N*, up to the next-higher power. This will limit the edge effects and speed up the Fourier transform. The zeros which have been entered the time-series will be removed after wavelet transform is finished [2].

Zero-padding of the time-series decreases the amplitude near the edges. For higher frequencies, where the periodicity of the signal is much less compared to the total time of the time-series, more zeros will be added to the ends and so the edge effects become more pronounced.

4.3. Wavelet choices

There are many commonly used wavelets that can be grouped into two main categories: Continuous Wavelets and Orthogonal Wavelets. It must be mentioned that a discrete wavelet transform may not be orthogonal. In orthogonal wavelet analysis, the number of convolutions at each scale is proportional to the width of the wavelet basis at that scale. The continuous transform is useful for time series analysis, where smooth, continuous variations in wavelet amplitude are expected [3]. One of the most widely used continuous wavelets in geophysics and climatology is *Morlet* wavelet,

$$\psi(\eta) = \pi^{1/4}\, e^{ik\eta}\, e^{-\eta^2/2} \qquad , Morlet \qquad eq. 7$$

which consists of a plane wave modified by a Gaussian envelope. The parameter k is a nondimensional frequency. In order for equation 7 satisfy the admissibility condition, k must be equal or greater than 6 [5].

Another commonly used continuous wavelet is the *DOG (Derivative of Gaussian)* which is the second derivative of the Gaussian function,

$$\psi(\eta) = \frac{-1^{k+1}}{\sqrt{\Gamma\left(k+\frac{1}{2}\right)!}} \frac{d^k}{d\eta^k}\left(e^{-\eta^2/2}\right) \qquad , DOG \qquad eq. 8$$

The Derivative of Gaussian wavelet with k = 2 is also known to as the “Mexican hat” wavelet.

The *Paul* wavelet is another continuous wavelet which is widely used when a high time localization is desired.

$$\psi(\eta) = \frac{2^k i^k k!}{\sqrt{\pi(2\pi)!}} 1 - i\eta^{-(k+1)} \qquad , Paul \qquad eq. 9$$

The simplest orthogonal wavelet is the *Haar* wavelet which is a based on a box function. The disadvantage of the Haar wavelet is that it is not differentiable. This property can, however, be an advantage for the analysis of signals with sudden transitions [6].

$$\psi(\eta) = \begin{cases} 1 & 0 \le \eta < \frac{1}{2} \\ -1 & \frac{1}{2} \le \eta < 1 \\ 0 & otherwise \end{cases} \qquad , Haar \qquad eq. 10$$

The use of these wavelets for different purposes is arbitrary. Since a true physical signal should be independent of the choice of the wavelet, one may use an analytical wavelet that bears reasonable resemblance in form to the signal [2]. In general, orthogonal wavelets are used in decomposition and in reconstruction of time series with *minimal bases*, and in signal processing as they give the most compact representation of the signal. The continuous wavelets, on the other hand, are useful for time series analysis, where smooth, continuous variations in wavelet amplitude are expected [3]. Hence, the orthogonal wavelets are better used for synthesis and data compression, while continuous wavelets are better used for time-series analysis.

One of the objectives of this master thesis, as mentioned in the introduction, is looking for short-term periodic signatures in solar irradiance at 280 nm. For this purpose, we will concentrate on the continuous wavelets *Morlet* and *Paul*, which as discussed in the last paragraph, are widely used in scale analyses. But before starting to talk about the differences between these two wavelets and their application, it is useful to see how a wavelet transform is performed.

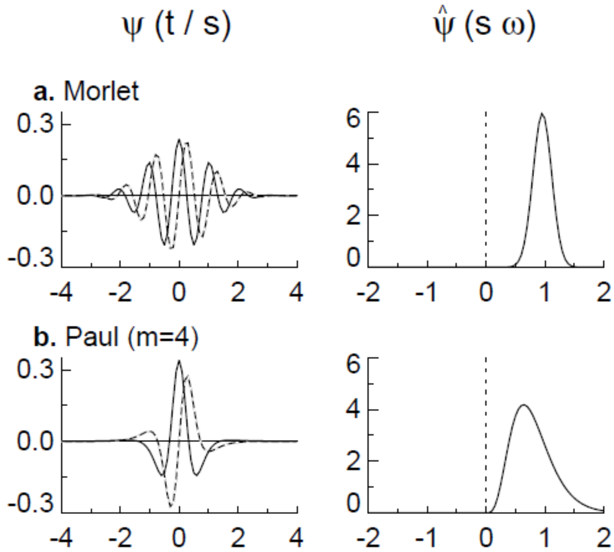

Fig. 4.2. Morlet and Paul Wavelet

The plots on the left give the real part (solid) and imaginary part (dashed) for the wavelets in the *time domain*. The plots on the right give the corresponding wavelets in the *frequency domain*.[3]

4.4. Wavelet Transform procedure

The wavelet analysis is performed by decomposing the one dimensional time-series into two dimensional time-frequency space. The data is processed at different scales giving information on occurrence of a frequency band in a certain time interval. Wavelet transform is a convolution, and a convolution is basically a mathematical operation on two given functions, producing a third function that is typically viewed as a modified version of one of the original functions. In case of the wavelet function, the two initial functions are the signal and the mother wavelet and the third function is the power spectrum.

Assume that we have a finite time-series. We then choose a wavelet with a pre-defined scale (frequency) and compare it to the first section (time interval) of the time-series (figure 4.3 a). Then we calculate how well are they match together. This quality is shown by the coefficient *C*. The coefficient is highly dependent on the shape of the wavelet (*Morlet, Paul, etc*). The next step is shifting the wavelet to the adjacent section and repeating the first two steps. This step continues until the whole time-series will be covered with the wavelet (figure 4.3 b). Now we step up into the next scale (let say the higher frequency) and repeat all previous steps for the new scale (figure 4.3 b). This procedure is carried on for all scales. Finally what we'll have is a series of coefficients produced at different scales by different sections of the signal corresponding to successive time intervals. We can now adopt colors to coefficients and plot them in a frame with x-axis representing the time domain and y-axis representing the scale or frequency domain.

It is obvious that for higher frequencies, the wavelet is more stretched and can measure only the coarser features of the signal, and lower frequencies it is more compressed and is able to measure rapid variations in the time-series.

Small scale > Compressed wavelet > Rapidly changing details > High frequency
Large scale > Stretched wavelet > Slowly changing, coarse features > Low frequency

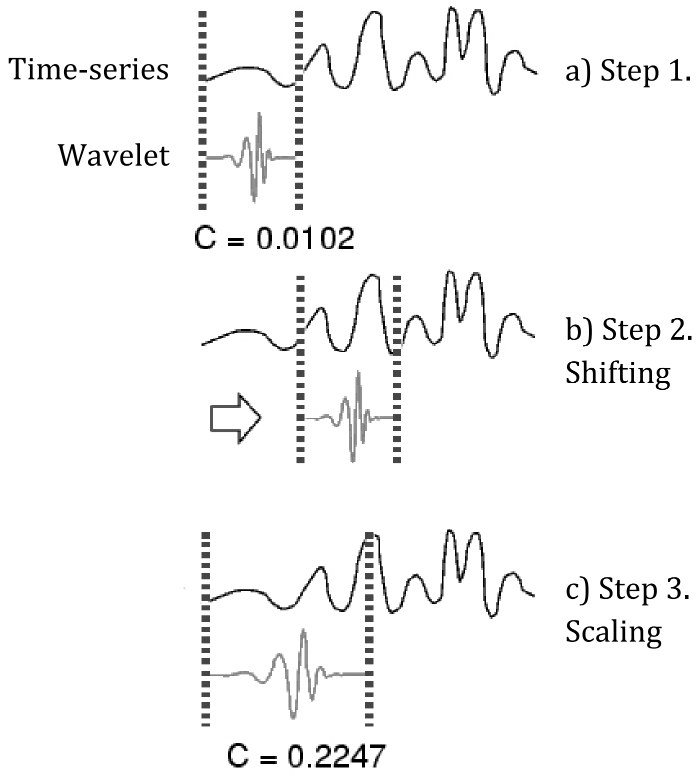

Fig. 4.3. Illustration of successive steps of Wavelet Transform of a given time-series [7]

4.5. Time and Frequency resolution

As discussed before, there are many choices for the wavelet analysis. In addition, a very important parameter that can affect the quality of the wavelet transform is the wavelet parameter indicated by k (introduced in equation 7). Basically, the value of k controls the number of oscillations present in the mother wavelet and, hence, will strongly influence the frequency and time resolution of the corresponding wavelet transform [4]. In figure 4.2, one can recognize that the Morlet wavelet has a large number of oscillations in the time domain and a narrow symmetric peak in the frequency domain, which will ensure a good frequency resolution. The Paul wavelet, on the other hand, has fewer oscillations in time domain and a wider anti-symmetric peak in frequency domain. This will give it a very accurate time resolution, and at the same time, a reduced frequency resolution.

The effect of varying wavelet parameters of two mother wavelets, *Morlet* and *Paul*, on the resulting wavelet transform of a given analytical function can be investigated trough a simple example. Suppose we have a function as defined bellow:

$$f(t) = \begin{cases} \sin(2\pi 10t) & 0 \le t < \frac{1}{4} \\ \sin\left(2\pi 25t + \frac{\pi}{2}\right) & \frac{1}{4} \le t < \frac{1}{2} \\ \sin\left(2\pi 50t - \frac{\pi}{2}\right) & \frac{1}{2} \le t < \frac{3}{4} \\ \sin\left(2\pi 100t + \frac{\pi}{2}\right) & \frac{3}{4} \le t < 1 \end{cases} \qquad eq.11$$

The phase shift of π/2 was included to ensure a continuous transition of phase. The function $f(t)$ is illustrated in figure 4.4. The wavelet transform of $f(t)$ is also illustrated in figure 4.5. From the figure, it appears that the Morlet wavelet resolves the different frequency components well, but there are some overlaps between their respective time localizations. For the Paul wavelet, the opposite seems to happen. There is a relatively sharp transition between the time localizations of the different frequency components, but the frequency resolution appears to be lower.

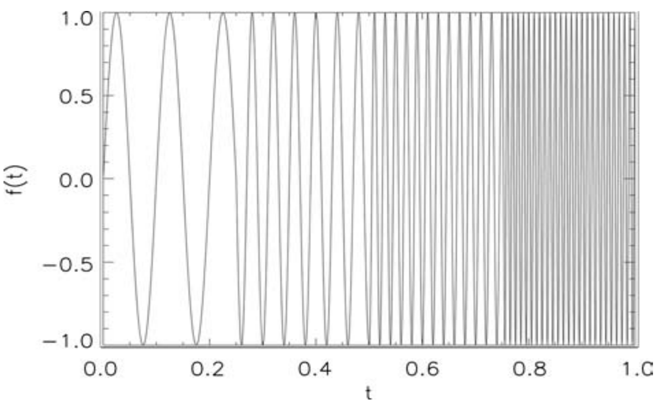

Fig. 4.4. The analytical function, f (t), defined in Equation 11, as a function of time [1]

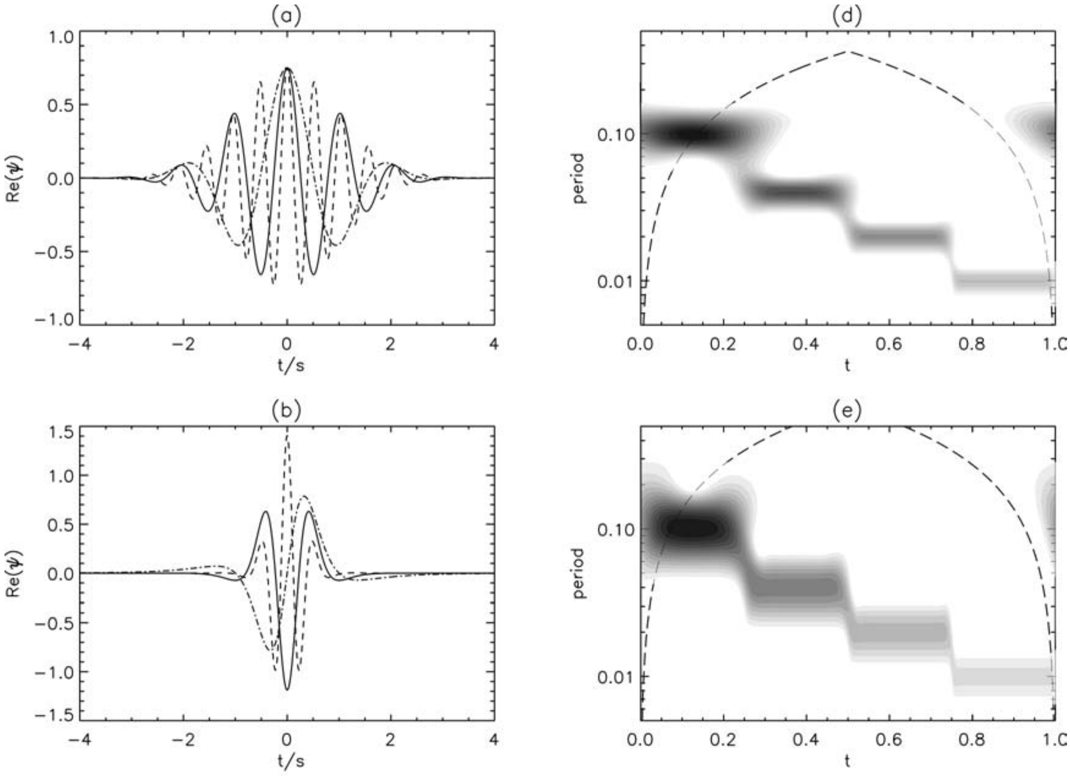

Fig. 4.5. (a,b) Morlet and Paul mother wavelets for different values of k (dot-dashed line: k = 3; solid line: k = 6; dashed line: k = 12). (e,f): corresponding wavelet transforms (k = 6) of the signal given in Equation 11 [1]

The effect of varying the wavelet parameter is even more pronounced. Figure 5.6 shows both the Morlet and Paul transforms of $f(t)$ for different values of k to investigate how the value of the wavelet parameter affects the resolution of the wavelet transform. In the figure, panels (a) and (b) show the Morlet and Paul wavelet transform with k = 3, respectively. It seems that there are no great differences between both transforms, apart from the slight lack of frequency resolution in the Paul wavelet, which was already noted in Figure 5.4 (k = 6). Panels (c) and (d) show the same transforms but for a large value of the wavelet parameter, k = 12. It is absolutely clear that there now is a big difference between the Morlet and Paul wavelets. For this large value of k, almost all time localization is lost in the Morlet transform, but the frequency resolution is extremely good. In the Paul wavelet transform, on the other hand, the frequency resolution has improved somewhat, without losing too much of the time localization.

Overall, Figures 5.5 and 5.6 shows that a better frequency resolution is obtained for larger values of k and by using Morlet wavelet, whereas a better time resolution is achieved for smaller values of the wavelet parameter and by applying Paul wavelet.

In this study, the higher resolution in frequency domain is desirable, for it can indicate low frequency periodic signatures throughout the time-series. The continuous wavelet transform has been carried out using “wavelet code for IDL” written by Torrence and Compo (1998).

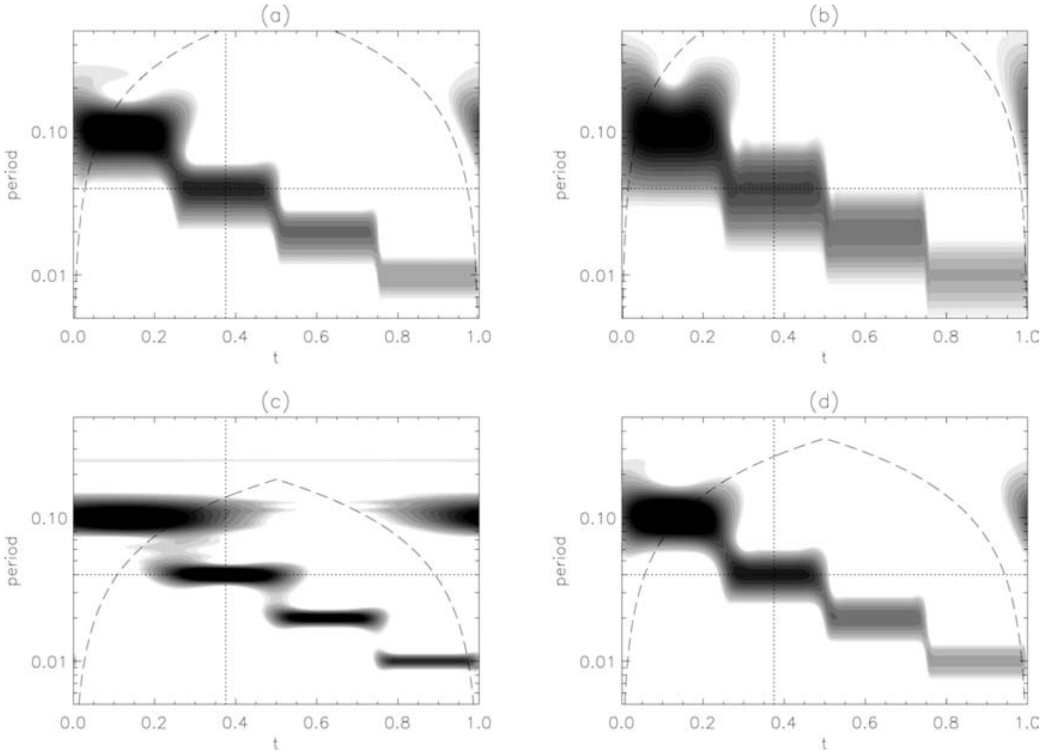

Fig. 5.6. Effect of varying wavelet parameter of the Morlet and Paul wavelets in wavelet transform. [1]
(a) Wavelet transforms of the signal f(t) using the Morlet wavelet with k = 3. (b) Equivalent result for the Paul wavelet with k = 3. (c) Equivalent result for the Morlet wavelet with k = 12. (d) Equivalent result for the Paul wavelet with k = 12.

References:

1. De Moortel, S. A. Munday and A. W. Hood: ***Wavelet Analysis: The Effect of Varying Basic wavelet Parameters***; *Sol. Phys. Volume 222, Number 2, pp. 203-228 (2004)*

2. K. M. Lau, H. Weng: ***Climate Signal Detection using Wavelet Transform: How to Make a Time Series;*** *NASA/Goddard Space Flight Center, Maryland; Des 1995*

3. Christopher Torrence and Gilbert P. Compo: ***A Practical Guide to Wavelet Analysis;*** *University of Colorado, Boulder, Colorado; Bulletin of the American Meteorological Society: Vol. 79, No. 1, pp. 61–78. (1998)*

4. Daniel T. L. Lee, Akio Yamamoto: ***Wavelet Analysis: Theory and Applications;*** *Hewlett Packard Journal; (1994)*

5. M. Farge: ***Wavelet transforms and their applications to turbulence***; *Annu. Rev. Fluid Mech, Vol. 24: 395-458 (1992)*

6. B. Lee, Y.S. Tarng: ***Application of the discrete wavelet transform to the monitoring of tool failure in end milling using the spindle motor current***; *The International Journal of Advanced Manufacturing Technology, Volume 15, pp. 238-243 (April, 1999)*

7. *The MathWorks, Inc. (http://www.mathworks.cn/access/helpdesk/help/toolbox/wavelet/ch01_i10.html#1000637) /wavelet/ch01_i10.html#1000637)*

As mentioned in the introduction, this study follows two main objectives: producing a long-term time series of the magnesium II index from 1978 to 2010 and looking for short-term periodic signatures in the time series. The first step is to produce a single time series of Mg II index by combining the data from various instruments. The Mg II data have been provided by many instruments. The data from several SBUV satellites (resolution ~1 nm) were originally combined to form a single time series by Donelly *et al. (1994)* and was extended to 1998 by *Viereck and Puga (1999)*. The Solar Ultraviolet Spectral Irradiance Monitor (SUSIM) experiment on the Upper Atmosphere Research Satellite (UARS) has produced similar Mg II observations at 1.1 nm spectral resolution from 1991 to 2005 *(Brueckner et al., 1993, Floyd et al., 1998)*. Higher spectral resolution measurements (0.24 nm) were made by the SolarStellar Irradiance Comparison Experiment (SOLSTICE) *(Rottman et al, 1993)* also on UARS from 1991 to 2000. Later, the Mg II data from Global Ozone Monitoring Experiment (GOME) on the European ERS2 satellite at 0.2 nm resolution were provided by *Weber et al. (1997, 1999).* And finally, the Mg II data from SCIAMACHY have been studied and validated with other instruments *(Skupin et al., 2005)*. In this work, the SCIAMACHY Mg II data based on Version 7 level 1 data was added to the data from the other instruments to produce a composite time series from November 1978 to June 2010.

Having the complete time series, the next step is to analyze it by different tools to point out any short-time periodic features corresponding to the 27-day solar rotation and its harmonics. These tools are Fast Fourier Transform (FFT) and Continuous Wavelet Transform (CWT). All data analyses have been done in Linux environment and by using IDL programs.

5.1. Producing Mg II time series

As mentioned in chapter 2, the Mg II index is derived by dividing the core value to the wing value of the Fraunhofer line around 280 nm. Figure 5.1 illustrates the solar irradiance in the wavelength interval between 275 nm to 285 nm, using GOME observations on 1st April 2000 when the solar cycle 23 is in maximum (top left) and on 1st April 2009 when it is in minimum (top right). The difference between core values is significant however the wing values are roughly the same for both solar maximum and minimum. In the bottom panel, the difference between two spectra is recognizable.

There are three ways to define the Mg II index. In the first definition, wing and core values are determined by averaging over the values of certain pixels (Skuplin et al., 2005). For example in case of GOME, the wing value (or background reference) is defined as the mean of the maxima of four parabolas corresponding to the data pixels (342, 344, 402, 404) (wavelengths 276.571, 276,791, 283.151, 283.369 nm) and the core value is defined as the mean of the maxima of two parabolas corresponding to the data pixels 371, 375 (wavelengths 279.759, 280.198 nm) all in channel 1A.

In another definition which has been introduced by Weber (1999), again in case of GOME, the wing value is defined as the mean of the maxima of four parabolas fitted thru the data pixels 335-339 (275.79-276.23 nm), 340-344 (276.34-276.79 nm), 400-403 (282.92-283.25 nm) and 407-4011 (283.69-284.12 nm) and the core value is given by sum of integrated intensities of the emission core lines. This is done by interpolation of the data points at one hundredth of the sampling size (which is 0.11 nm) and integration over a range of about 0.2 nm about both maxima (Weber, 1999). The benefit of this definition compare to Skuplin definition is that in case of any shift in the data set, we still have the correct values correspond the desired wavelengths. The third definition which is known here as the classical definition, has been given by Heath and Schlesinger (1986). Here again we have the same method to determine the wing value, but for the core value, we select three maxima instead of two, and then average over these three maxima. The reason is that in order to make the GOME and SCIAMACHY data sets comparable to SBUV data sets (which have much lower spectral resolution),

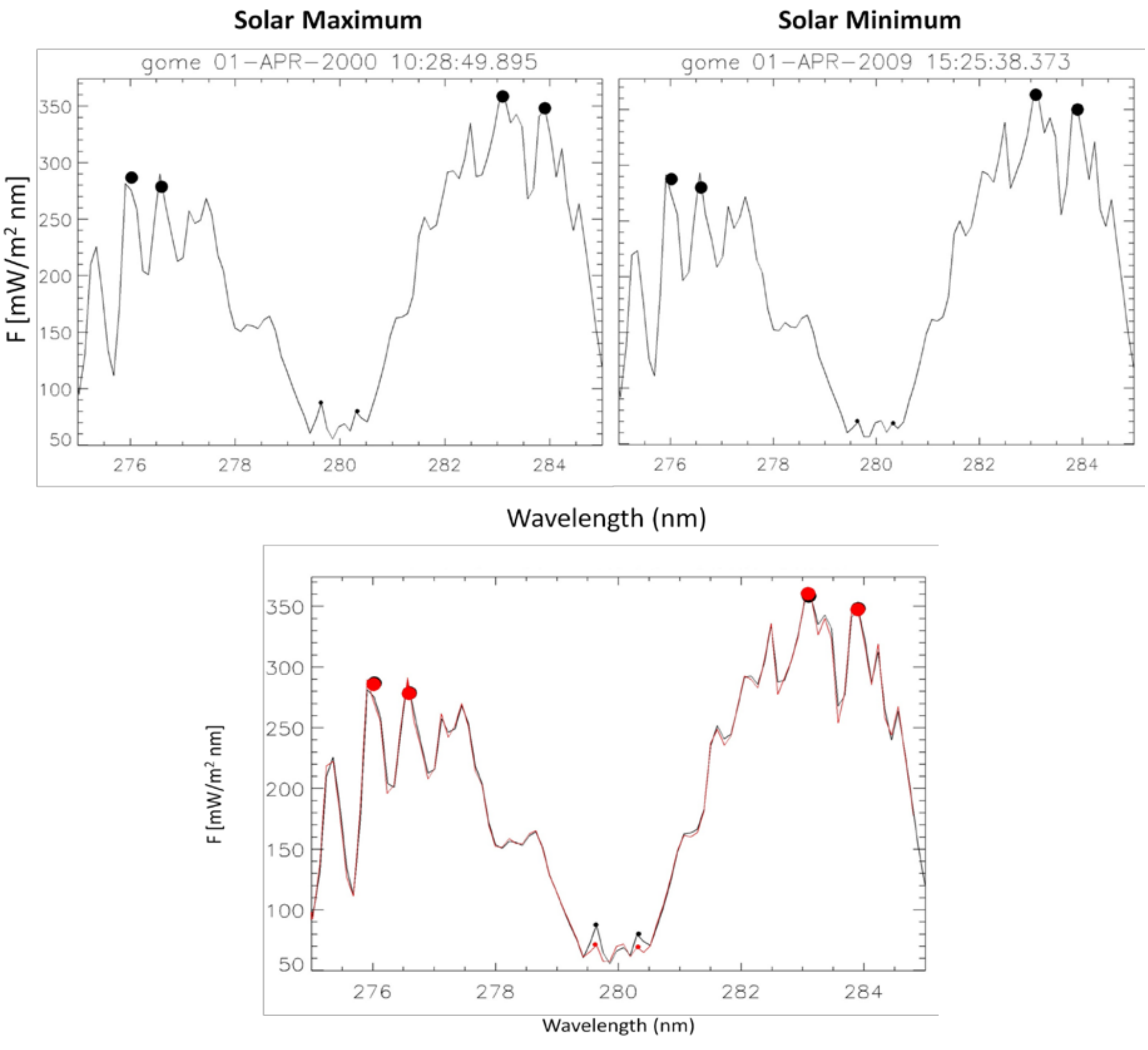

Fig 5.1. (top left) The MgII doublet at 280 nm recorded by GOME on April 1st, 2000 (top left) and 2009(top right). Bottom: The red line corresponds to the solar minimum irradiance at top- right and the black line corresponds to the solar maximum irradiance at top-left

the time series of these two instruments should be somehow smoothed. This can be done by a double smoothing procedure with an 11-pixel running average. The 11-pixel running average results in a 1.1 nm spectral resolution which is equal to SBUV spectral resolution. The smoothing function is:

$$R_i = \begin{cases} \frac{1}{w}\sum_{j=0}^{w-1} A_{i+j-w/2} & i = \frac{w-1}{2}, \dots, N - \frac{w-1}{2} \\ A_i & otherwise \end{cases} \qquad eq.12$$

In which A represents the series of data points (time series), i is the array index and w is the smoothing width which was set to 11 for smoothing the GOME and SCIAMACHY time series. The ASCII code used for this purpose in IDL is:

pixel=**smooth**(**smooth**(*pixel*,11),11)

The smooth function returns a copy of the array smoothed with a boxcar. The instrument function of the SBUV instruments is a triangular function, which is the same as a convolution of two boxcars. Hence the double smoothing which is introduced above results in a triangular function. The smoothed (or classical) Mg II time series from these two instruments are illustrated in Figure 5.2.

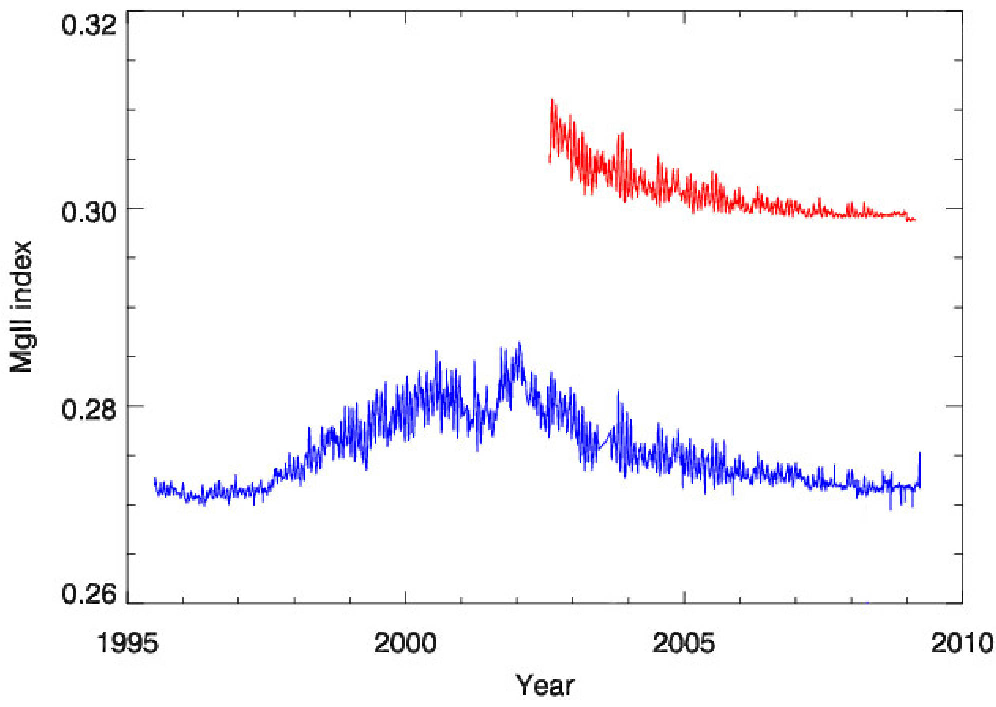

Fig 5.1. Classical Mg II time series from GOME (blue) and SCIAMACHY (red)

At the first glance, it can be recognized that the GOME time series is noisier particularly in recent years, while the SCIAMACHY time series, especially close to the solar minimum is very smooth and flat. There is also a small abrupt step in SCIAMACHY time series in December 2009 which might be due to the instrument decontamination

carried out during that time. The noise in the GOME data is due to decreasing signal-to-noise related to the optical degradation of the instrument with time.
The production of the Mg II index from GOME and SCIAMACHY measurements was an important part of this study. The Mg II data of other instruments were provided from other sources. Each of the data sets and analysis procedure results in a unique range and set of values. Figure 5.3 shows the original values of ten Mg II data sets plotted together. The differences are due to various instrument resolutions and analysis techniques. To produce the final composite, a combination of these time series was used.

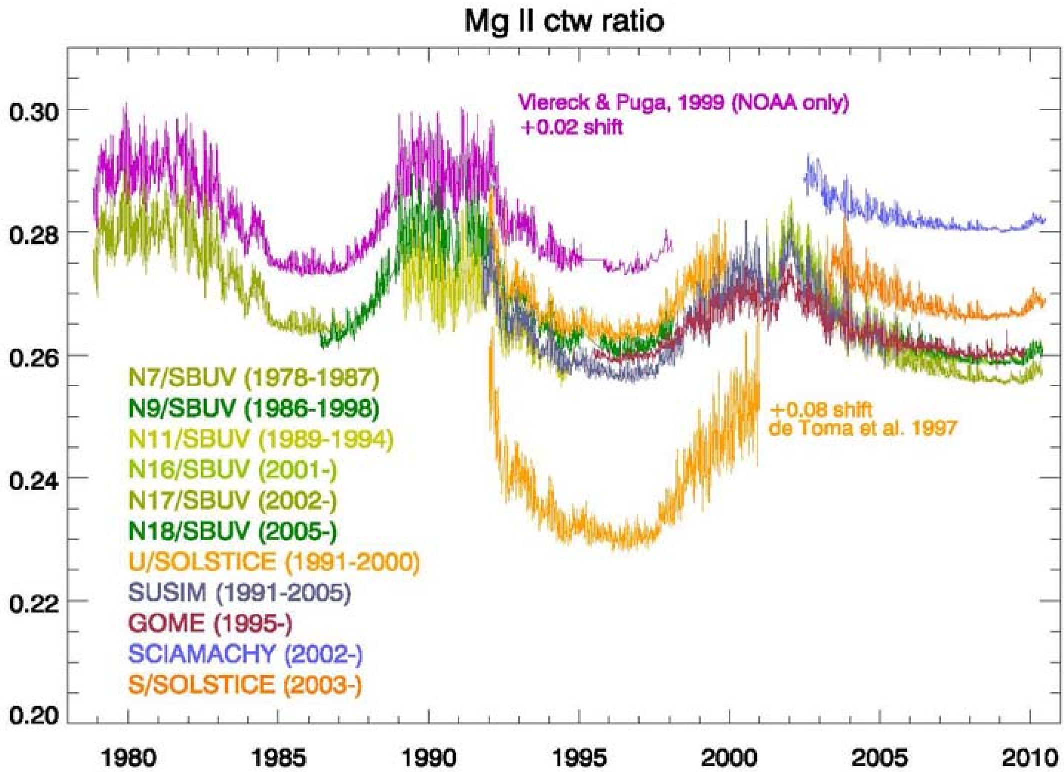

Fig. 5.3. Mg II data sets from different instruments. NOAA times series is the composite of N7, N9, and N11 as contained in the overall composite from Viereck et al. (2004). They are different than the one available at http://sbuv2.gsfc.nasa.gov/solar/ by Matt deLand, personal communication (see data sets numbered 2 to 4 in Table 5.1).

Inst. ID	Instrument name	Contribution to final time series
1	NOAA (Viereck and Puga et al., 1999)	3911
2	N7/SBUV	50
3	N9/SBUV	10
4	N11/SBUV	18
5	N16/SBUV	110
7	N18/SBUV	1
8	U/SOLSTICE (de Toma et al.)	1367
10	SUSIM	102
11	GOME	2515
12	SCIAMACHY	2465
13	S/SOLSTICE (Classic)	104
14	F10.8	914

Table 5.1. Contribution of each instrument in final composite time series

The process of combining the time series begins with choosing the data sets which are overlapping across the time frame. These data sets will be then linearly scaled to each other and so one obtains the individual contribution of each time series to the final time series. For periods where no Mg II data is available, especially for the measurements between 1978 and 1991, the F10.7 cm data can be used to fill the gaps. The data gaps after 1991 are mostly filled using the remaining data from other instruments. Table 5.1 shows the number of data points from each instrument in the final time series. The problematic issue in terms of scaling is to choose a time series as the reference to scale all other time series to it. This is an absolutely arbitrary choice and the priorities of the data sets can be altered based on the result of the further analyses, so that the best result (with respect to expectations), determines the best configuration of the data sets. The scaling procedure starts by reducing the two time series to the overlapping time period. This reduction is shown in figure 5.4 for GOME and SCIAMACHY (for which the overlapping time starts in 2002). Now the reduced time series have the same number of data points and can be linearly fitted. For this purpose we use the LINFIT function in IDL. The LINFIT function fits the paired data {e.g. x_i, y_i} to the linear model, $y = A + Bx$, by chi-square minimization. This will result in a two-element vector containing the linear model parameters $C=[A, B]$. Here y represents the reference time series (e.g. SCIAMACHY) and x represents the time series to be scaled and fitted (e.g. GOME). Hence the priority of the time series can be quite significant in terms of scaling because it can modify the model parameters. To reduce the effect of choosing the reference, a simple method can be applied. In this method, the fitting procedure is carried out two times, once by assuming y as the reference and once by letting x to be the reference. Now there are two vectors of model parameters $C=[A, B]$ and $C'=[A',B']$ available:

$$\begin{cases} y = A + Bx & \mathrm{C} = [\mathrm{A}, \mathrm{B}] \\ x = A' + B'y \ \rightarrow \ y = \dfrac{-A'}{B'} + \dfrac{1}{B'}x & \mathrm{C}' = \left[\dfrac{-A'}{B'}, \dfrac{1}{B'}\right] \end{cases} \qquad eq.13$$

We have then two different parameter vectors for the same model ($y = \mathcal{A} + \mathcal{B}x$). By averaging over C and C', it is possible to find an optimized model parameter which minimizes the effect of choosing different references. The optimized fitting parameters are then used to scale the whole time series to the reference. These steps will be applied to all time series from the different instruments.

Comparing various cross correlations between time series illustrates several differences between them. Figure 5.5 shows a few of the more important cross correlations. These plots include the correlation coefficients, R, between various data sets. There are several points that can easily be made from Figure 5.5. First, the data sets are highly correlated, and the scatter plots are well approximated by linear functions, with R ranging from 0.982 to 0.992, with one exception where R equaling 0.83 is rather low, which will be discussed later. It is also clear that some data sets are, in general, noisier than others.

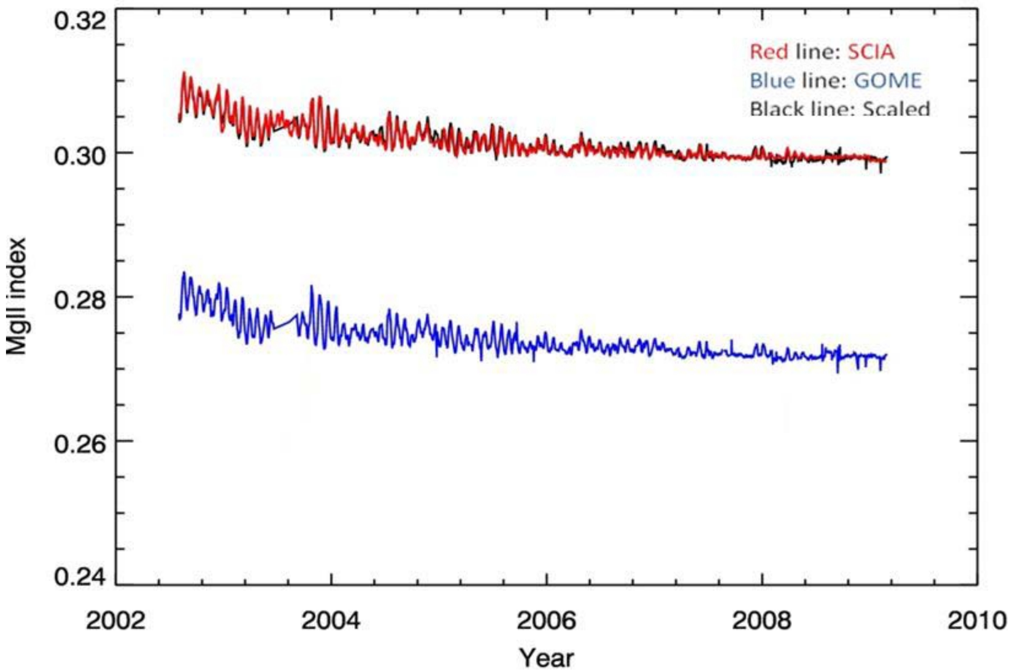

Fig. 5.4. Mg II index from GOME and SCIAMACHY from 2002 to 2009. The SCIAMACHY data set assumed to be the reference and the GOME data set is scaled and fitted to the SCIAMACHY time series.

From Figure 5.3 it can be seen that the N7 and N9 time series are overlapping for relatively very short time (the number of overlapping days, *n*, is mentioned at the top of each plot in Figure 5.5). Also this overlap between these two time series is during minimum solar activity, so the variations in Mg II index are very low. On the other hand, it is clearly recognizable from figure 5.3 that N9 time series starts in solar minimum and increases very sharply, while N7 is quite flat in the overlapping period. All these result in a low correlation coefficient between N7 and N9 which is equal to 0.838. In addition, among the six plots in Figure 5.5, the two fitting lines for five of them are very close, so the priority in choosing the reference data set between the pairs may not affect the final time series *significantly*, but there is an exception in case of N7 and N9. We can obviously see that if we choose N7 or N9 as the reference, the fitting lines will be show completely different trend. Here the significance of choosing the reference time series can be understood.

For other pairs, we see that the time series are quite correlated after taking out the bad data points. The cross correlation plot of GOME and SCIAMACHY shows some out-layers especially at the beginning of the scatterplot where the solar cycle is minimum. By comparing this plot with Figure 5.1, we can conclude that these data points are mostly from GOME data set which is much noisier during solar minimum.

By taking ratios between the scaled data sets, it is possible to identify additional features and, more importantly, any time-dependent drifts or changes in individual data sets. Figure 5.6 shows the ratios between some of the data sets. Most of the data sets in this figure and others which are not included in the figure are within 0.5% of each other, however the variations – long-term and annual - are quite different for each pair. From the plots in Figure 5.6 and similar plots of other ratios, it is possible to remove some of the problematic data.

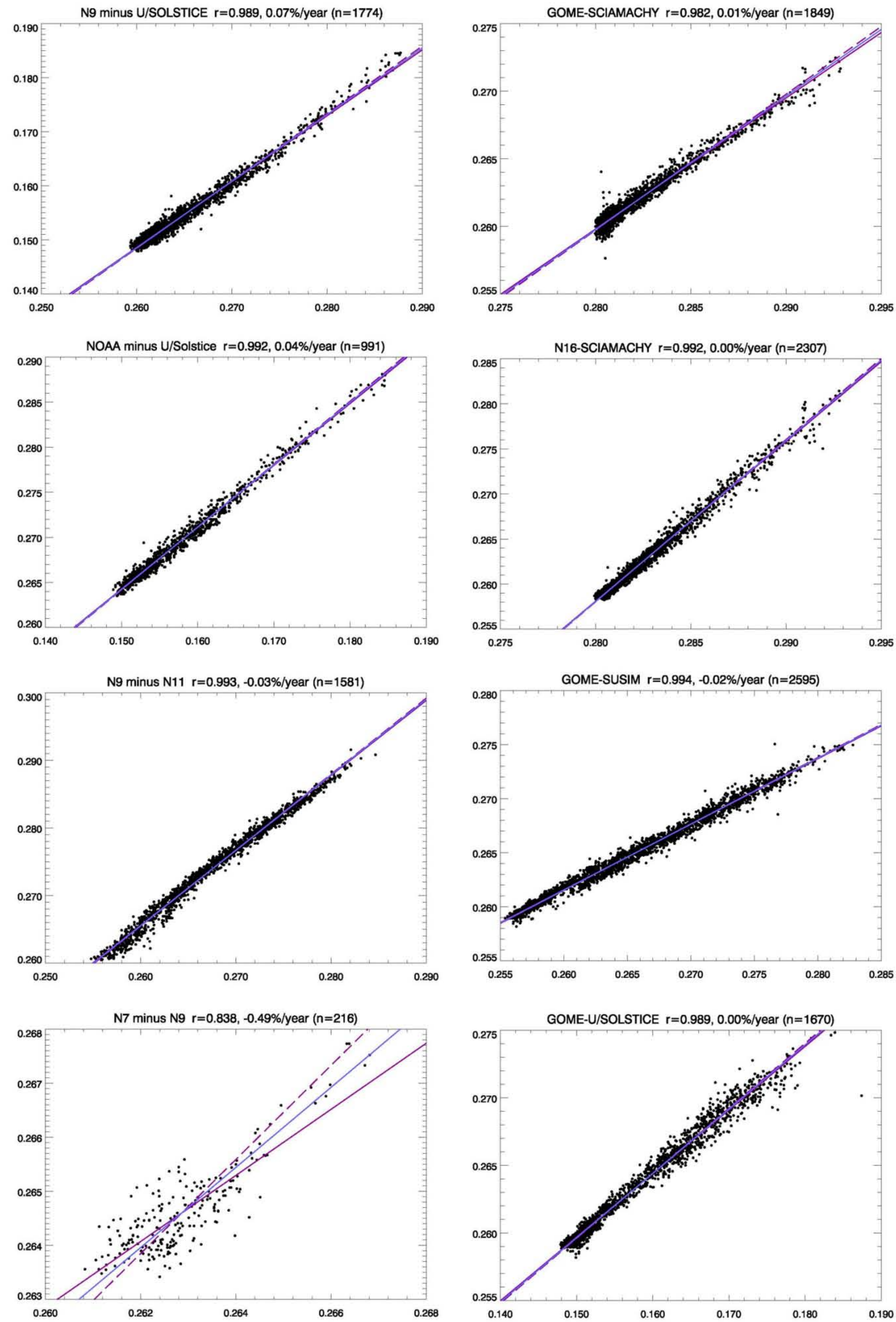

Fig. 5.5. Cross correlations between some of the data sets. The correlation coefficients, R, are listed at the top of each plot. The violet lines correspond to the two sets of fitting coefficients in equation 13 and the blue line is the unity line.

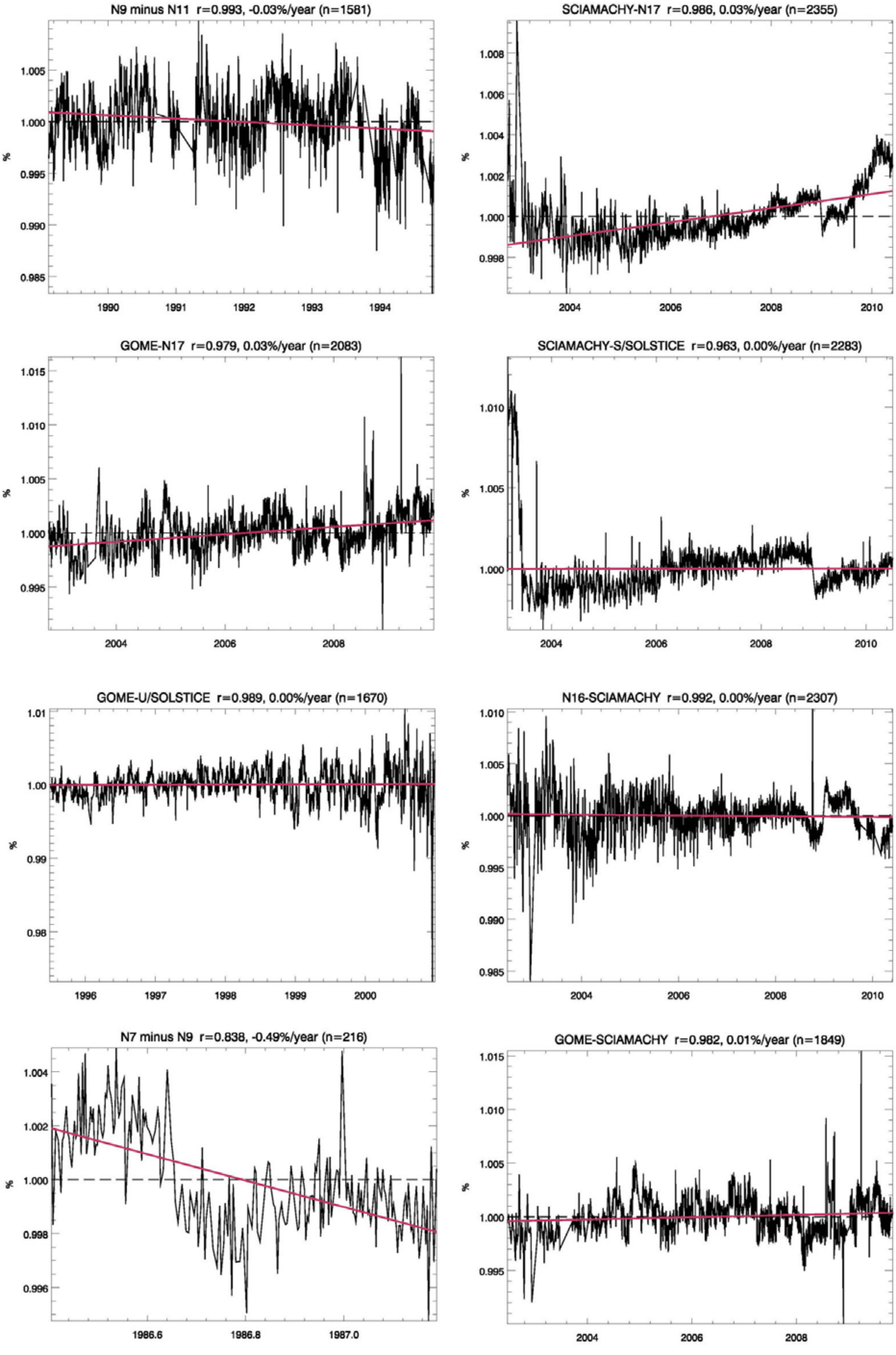

Fig 5.6. Ratios between various data sets. The red lines show the fitted linear trends.

For example, if there are three data sets for a given period, and one of them has an offset or trend, then two of the three ratios between these data sets will show this problem allowing the bad data set to be isolated. This situation can be seen between GOME, SCIAMACHY and N17. Again from the figure 5.6, the GOME/N17 and SCIAMACHY/N17 ratios show a higher trend as compared to GOME/SCIAMACHY ratio. This suggests that GOME has a higher priority than N17 (assuming SCIAMACHY to be the reference time series). However, by comparing GOME/N17 and GOME/SCIAMACHY ratios, we can see that there is a step at the beginning of 2007 and 2008, which is not visible in SCIAMACHY/N17 ratio. This immediately suggests that this step might be from GOME time series. SCIAMACHY/N18 ratio also shows a large positive trend. So this time series has also a lower priority. In fact, there are no data points from N17 and N18 in the final time series. Regarding N7 and N9, we have the same problem that we had in terms of cross correlations. Although the data sets are within 0.2% of each other, we can clearly see a time-dependent drift and a high negative trend. Unfortunately N7 is the only time series available for the first eight years of Mg II measurements, and there is no alternative available for this period. However, in some works, N7 measurements have been compared to F10.7cm flux in order to improve the reliability of N7 data sets. This was not done in this study.

After all, we have now a single time series by combining data from four main instruments: NOAA (Viereck and Puga mainly containing SBUV measurements from NIMBUS-7 and NOAA-9) from 1978 to 1991, UARS/SOLSTICE from 1991 to 1995, GOME from 1995 to 2002 and SCIAMACHY from 2002 to 2010. These time series were the reference data sets to which the other data sets have been scaled. Once the overall trends were defined by these four primary data sets, the gaps were filled with the remaining data. This contribution from other data has been already given in Table 5.1. The final composite time series, which is shown in Figure 5.7, consists of more than 11000 days of solar irradiance measurements covering three complete solar cycles from November 1978 to June 2010.

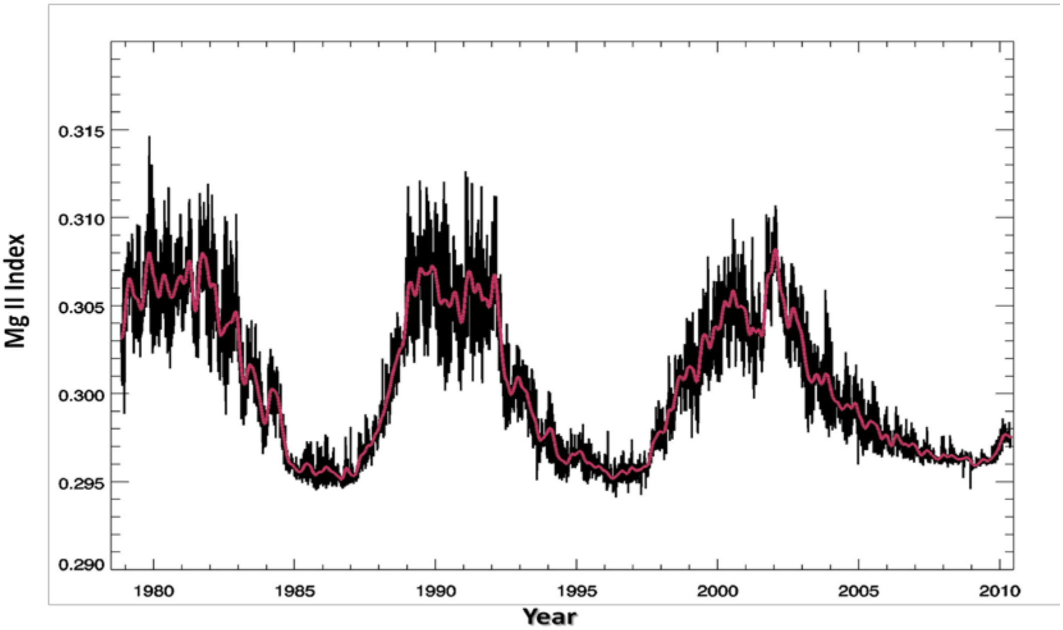

Fig. 5.7. Final time series of the Mg II from November 1978 to June 2010

There are several features of the Mg II Index, as shown in Figure 5.7, that should be pointed out. First, the solar cycles 21, 22, and 23 are very obvious and form the largest features in the time series. The maximum of the Mg II index is very similar for solar cycle 21 and 22, but slightly lower for cycle 23 compared to the two previous cycles. This is consistent with other proxies of solar activity such as sunspot number and F10.7 cm flux. The minimum of solar cycle 23 seems to be slightly higher than that of the two other cycles. This has not been seen in other studies in which a similar minimum for solar cycle 23 (in comparison with solar cycles 21 and 22) has been reported. Another interesting feature which can be seen in the time series is the start of the solar cycle 24 which occurred in October 2009. In the next section, FFT and WT analyses were applied to extract information on short-term periodic features from this long-term Mg II time series.

5.2. Periodic features in Mg II composite time series

As discussed in chapter 4, one of the best mathematical tools for signal analysis is the Continuous Wavelet Transform (CWT). Since the second objective of this study is investigate the short-term periodic features of the final Mg II time series, we will focus on the wavelet transform of the time series to extract the periodicities of these features. However, the Fast Fourier Transform of the time series can also provide useful information on the dominant frequencies in the final time series.

The CWT has been carried out using the "wavelet code for IDL" written by Torrence and Compo (1998). This program computes the CWT of a 1D time series. The ASCII code to call this program is:

WAVE = **wavelet** (Y=*mgii*, DT=*1*, MOTHER=*'morlet'* ,PARAM=*30*, DJ=*0.01*, SIGLVL=*0.90*, PERIOD=*period*, SCALE=*scale*, COI=*coi*, LAG1=*lag1*)

The inputs are 'Y' (the time series of length N) and 'DT' (amount of time between each 'Y' value, i.e. the sampling time). The output is 'WAVE' which is the wavelet transform of 'Y'. The wavelet power spectrum is then defined by 'ABS(WAVE)^2'. Here *mgii* is the time series and since the time series consists of daily Mg II measurements, the sampling time 'DT' is set to 1. The other variables are optional input keywords. The keyword 'MOTHER' is a string giving the mother wavelet to use. The Torrence and Compo program currently supports only 'Morlet', 'Paul' and 'DOG' (derivative of Gaussian) mother wavelets and the default is Morlet. 'PARAM' determines the wavelet parameter. 'DJ' defines the spacing between discrete scales. The default scale spacing is 0.125, however a smaller value will give better scale resolution, but the program runs slower. 'SIGLVL' determines the significance level which has been set to 0.90 in this work. 'PERIOD' and 'SCALE' keywords define the vectors of Fourier periods that correspond to the scales and scale indices, respectively. 'COI' returns the Cone-of-Influence, which is a vector of N points that contains the maximum period of useful information at a particular time. It is sometimes useful to calculate the autocorrelation of the time series at Lag-1 which is the correlation coefficient between the value of the time series at time t and its value at time t-1. This calculation is done by setting the keyword 'LAG1' in the ASCII code and the value of this variable for this time series is 0.98.

Figure 5.8 shows the CWT and FFT of the final time series. The CWT plot has been produced using a Morlet wavelet of order 30 ('PARAM'=30). Choosing the Morlet wavelet with a high parameter increases the resolution in the frequency domain (as explained in chapter 4), guaranteeing the exposure of the short-term periodic features in the time series. The 27-day signature (corresponding to the rotational period of the sun) can be clearly seen in both CWT and FFT plots.

In the CWT plot, the yellow line shows the 90% significance level. The dominant scales corresponding to this level of significance are the frequencies between 25 to 30 days. This is however not surprising as we know that this is approximately the rotational period of the sun. We can also see that the wavepower is highest at solar maxima. This is the significant property of wavelet transform; we can obviously see the frequency of the 27-day signal and simultaneously the localization of this signal in the time domain. Using the FFT of the Mg II time series, however, we can identify the dominant frequencies representing the entire time domain. The blue line at a period of 0.037/day corresponds to the 27 day signature. In fact this value on the horizontal axis determines the fraction of a cycle that happens in a day. For example, the peak at 0.037/day, means that there is a periodic signal in the time series whose 0.037 of its period happens per day, or in other words, it takes 27 days for the signal to make a complete cycle ($27\ day\ period \equiv 0.037 \frac{1}{day}\ frequency$).

In addition to this 27-day signal, we can see another periodic feature corresponding to a 13.5 day period. The wavepower at this scale (period) reaches significant levels in during solar maxima 21 and 22 around the years 1979 and 1992, respectively. Again we can clearly see the occurrence of this period in the FFT plot, i.e. the peak which corresponds to the 0.074/day frequency. This of course is an important outcome, for the 13.5 day signature has been rarely reported being seen in Mg II time series. The 13.5-day signature is the second harmonic of the 27-day signature. The nature of these periods is the existence of hot spots on the sun. As discussed in chapter 1, a hot spot is a group of faculae on the photosphere. The hotspots may appear in single or double systems and can exist during several solar cycles (Usoskin et al., 2005; Berdyugina, 2007). A double hotspot system is made of two hotspots that rotate with the same period but are separated by about 180° in longitude (Bai, 2003; Zhang et al., 2007), generating the 13.5-day periodicity in solar flux. The intensity of the two hot spots is changing with time, and there could be periods when they have the same intensity, creating a "pure" 13.5-day cycle (Fioletov et al., 2009). Both the 27 and 13.5 day signatures are illustrated by dashed-blue lines in the CWT plot in Figure 5.8.

Figure 5.9 shows the CWT and FFT of the Mg II time series using only GOME and SCIAMACHY measurements. This time series is produced in order to focus on GOME and SCIAMACHY measurements as they are the two of the main instruments in the composite time series and covers the time period from 2002 to 2009. In the composite time series the data gaps in this time period were filled by UARS/SOLSTICE and SUSIM

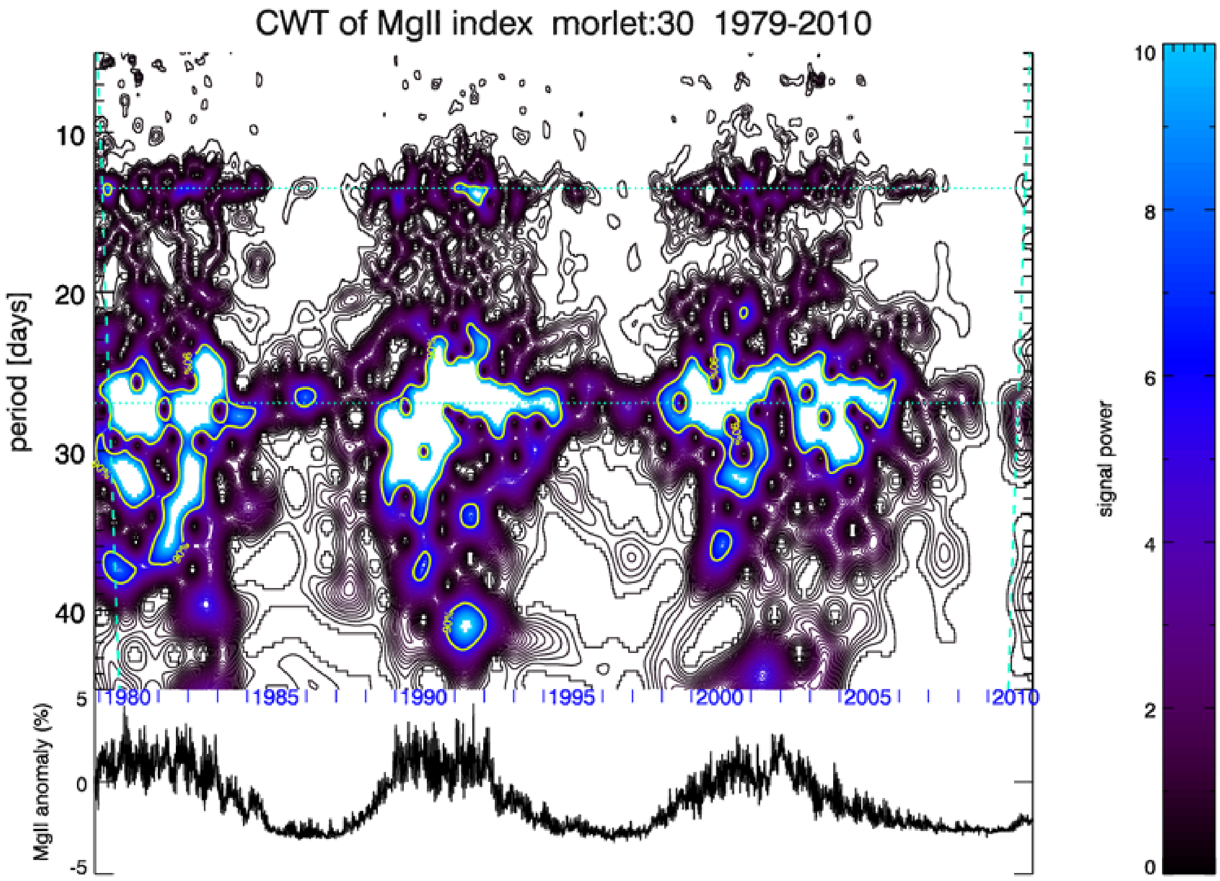

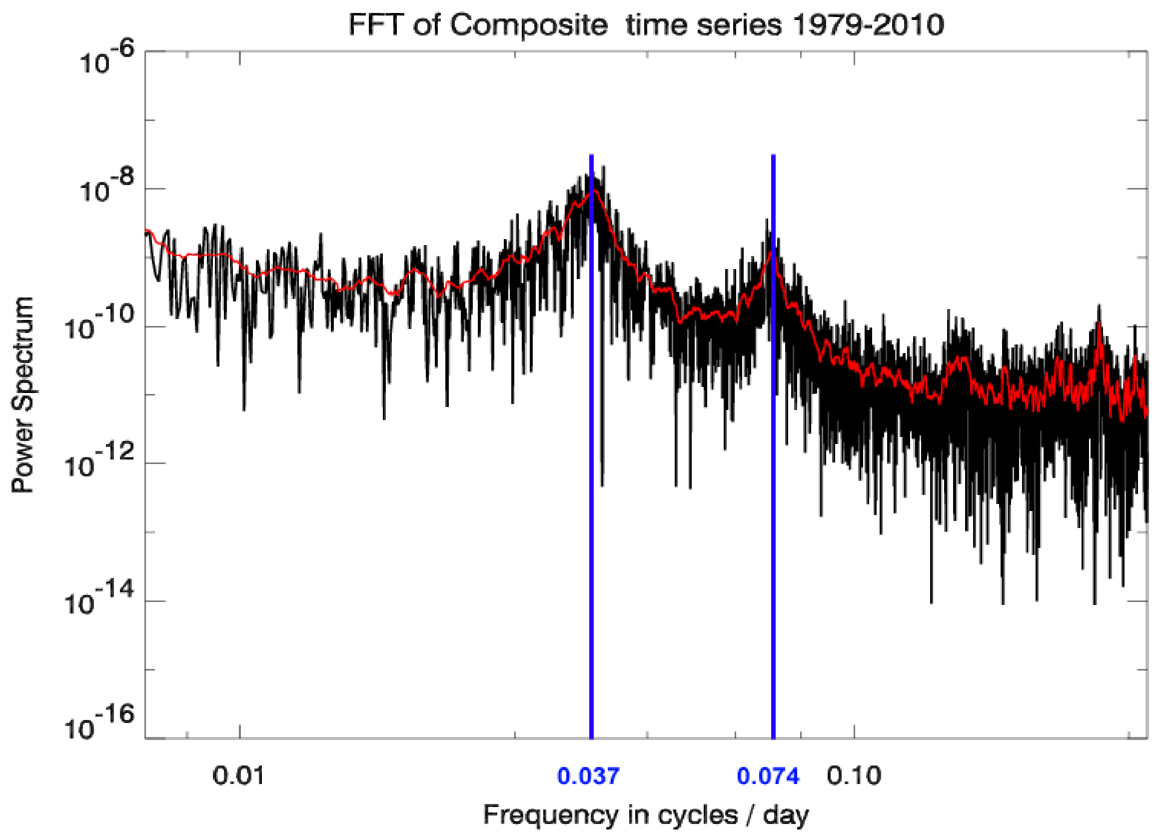

Fig. 5.8. The CWT (top) and FFT (bottom) of the composite Mg II time series. The red line represents the smoothed composite time series.

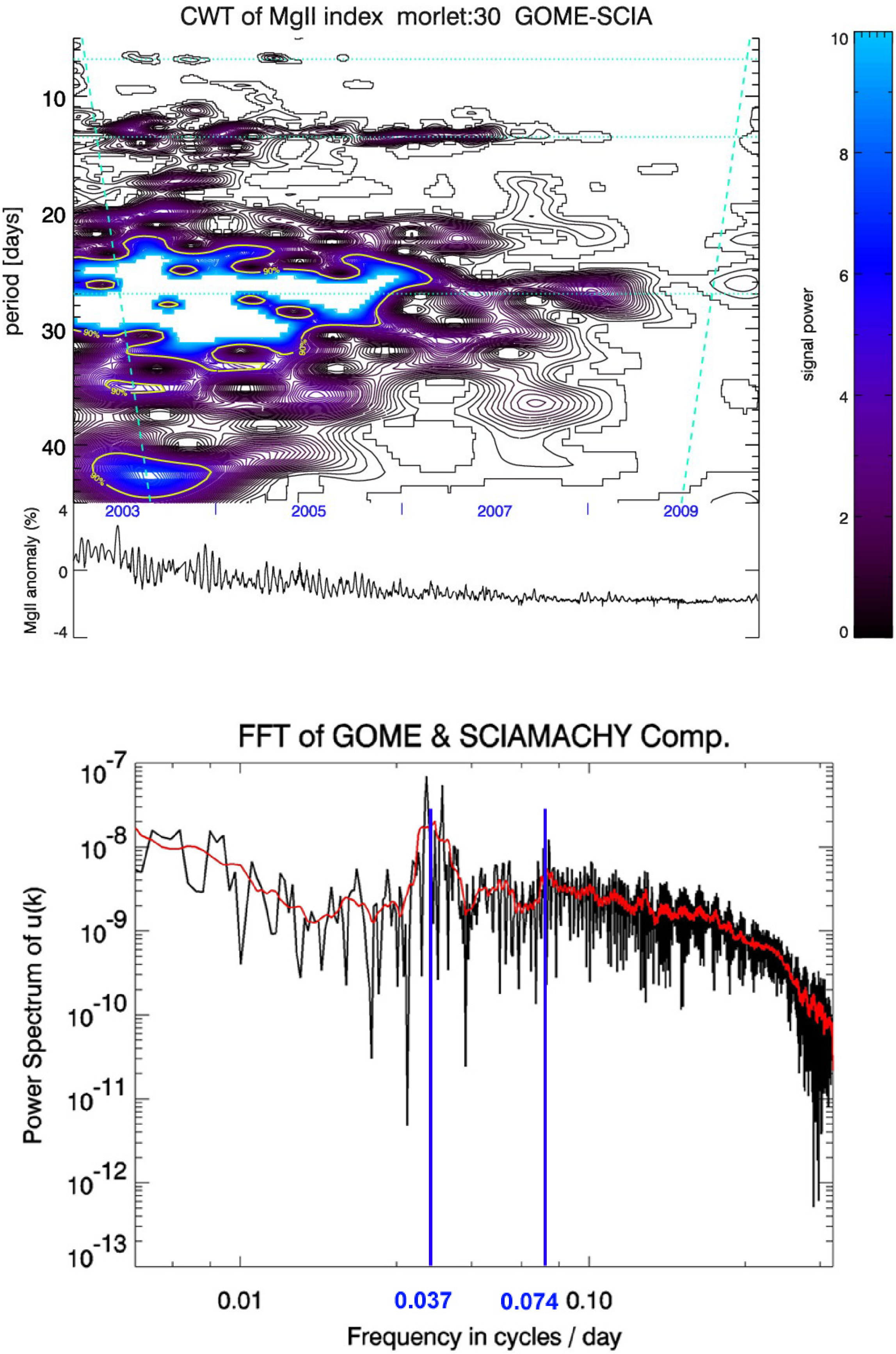

Fig. 5.9. The CWT (top) and FFT (bottom) of the GOME-SCIA Mg II time series. The red line represents the smoothed GOME-SCIA time series.

measurements, in the so-called GOME-SCIA time series the gaps have been filled by normal interpolation. Here again both the 27 and 13.5-day signatures are visible in the figure. The 13.5-day signature does not reach the significant level at 90%. The reason might be the lower solar irradiance at solar maximum 23 compared to solar cycles 21 and 22. Another interesting feature in the CWT plot is a significant level corresponding to the 40-day period. There is however no cyclic phenomena in the sun with a 40-day period. The occurrence of this periodic signal might be the superposition of the 27-day and 13.5-day signal which basically can produce a beating signal with a 40-day period. The two frequencies of 0.037 and 0.074 corresponding to 27 and 13.5-day signatures, respectively, are visible in FFT plot but with relatively lower amplitudes compare to that of the composite time series in Figure 5.8.

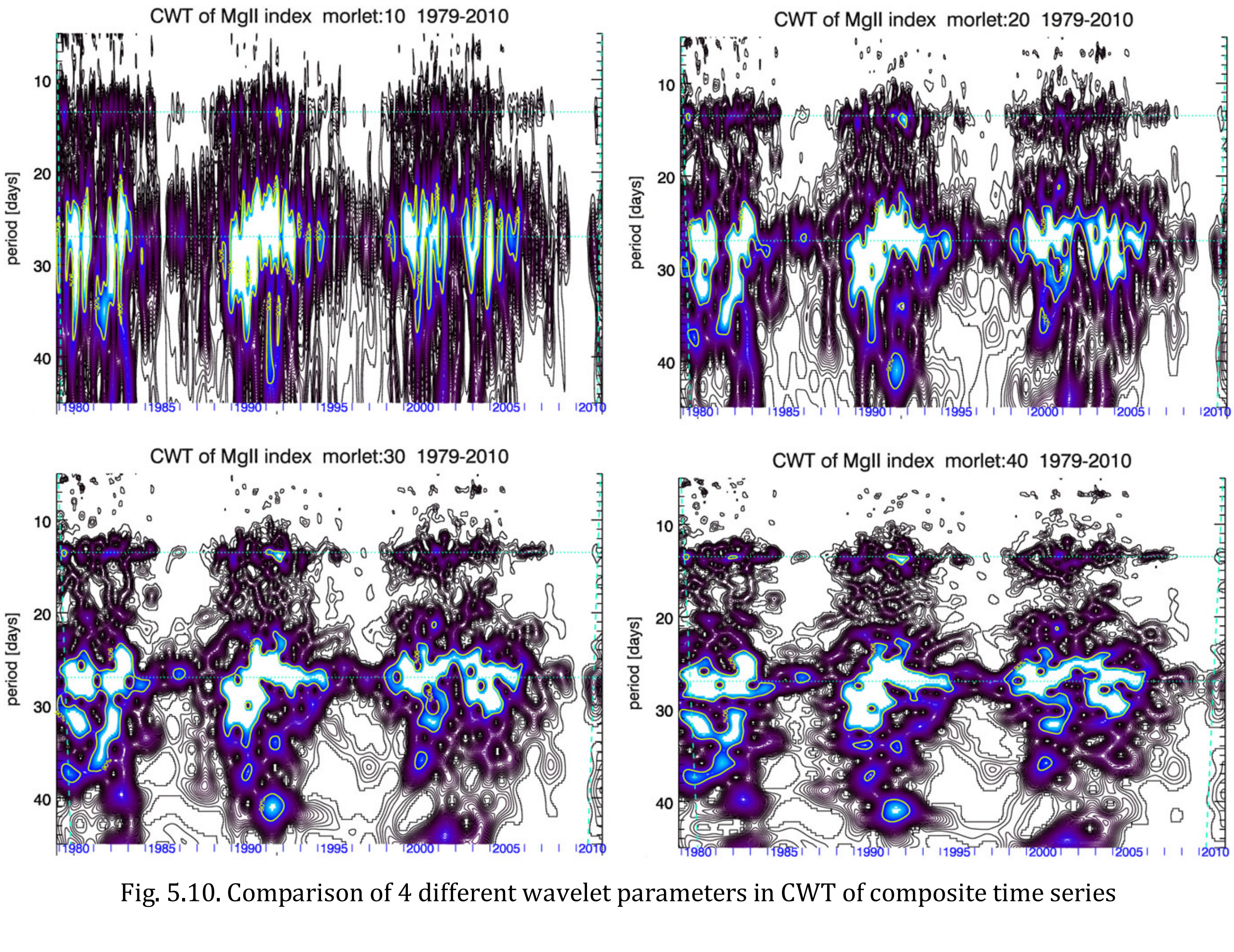

Fig. 5.10. Comparison of 4 different wavelet parameters in CWT of composite time series

In chapter 4, the effect of different wavelet parameters (order) on the wavelet transfer were discussed by giving an example. Now we can see how the CWT of the Mg II composite time series changes by applying different parameters. Figure 5.10 illustrates four different CWTs of the composite time series using Morlet wavelet with parameters equal to 10, 20, 30 and 40. As we expect, by increasing the wavelet parameter, the areas which have been indicated by the yellow contours (significant level equal to 90%) become narrower with respect to the period domain and wider in the time domain. Decreasing the wavelet parameter has exactly the reverse effect. The narrower contours with respect to any of the domains correspond to a resolution increase in that domain. The CWT with wavelet parameter equal to 40 has the best frequency resolution but the time localization is quite low.

By looking carefully at the CWT and FFT plots, another periodic feature can be recognized; an approximately 7-day periodic signal. Figure 5.11 illustrates this signal in both CWT (the upper blue line) and FFT of the final composite time series as well as the GOME-SCIA time series. Although the intensity of the solar irradiance at solar maximum 23 was less than that of the two previous maxima, the so-called 7-day feature is more visible at this solar maximum. The reason might be the enhanced spectral resolution of the instruments whose measurements have been used for this part of the time series.

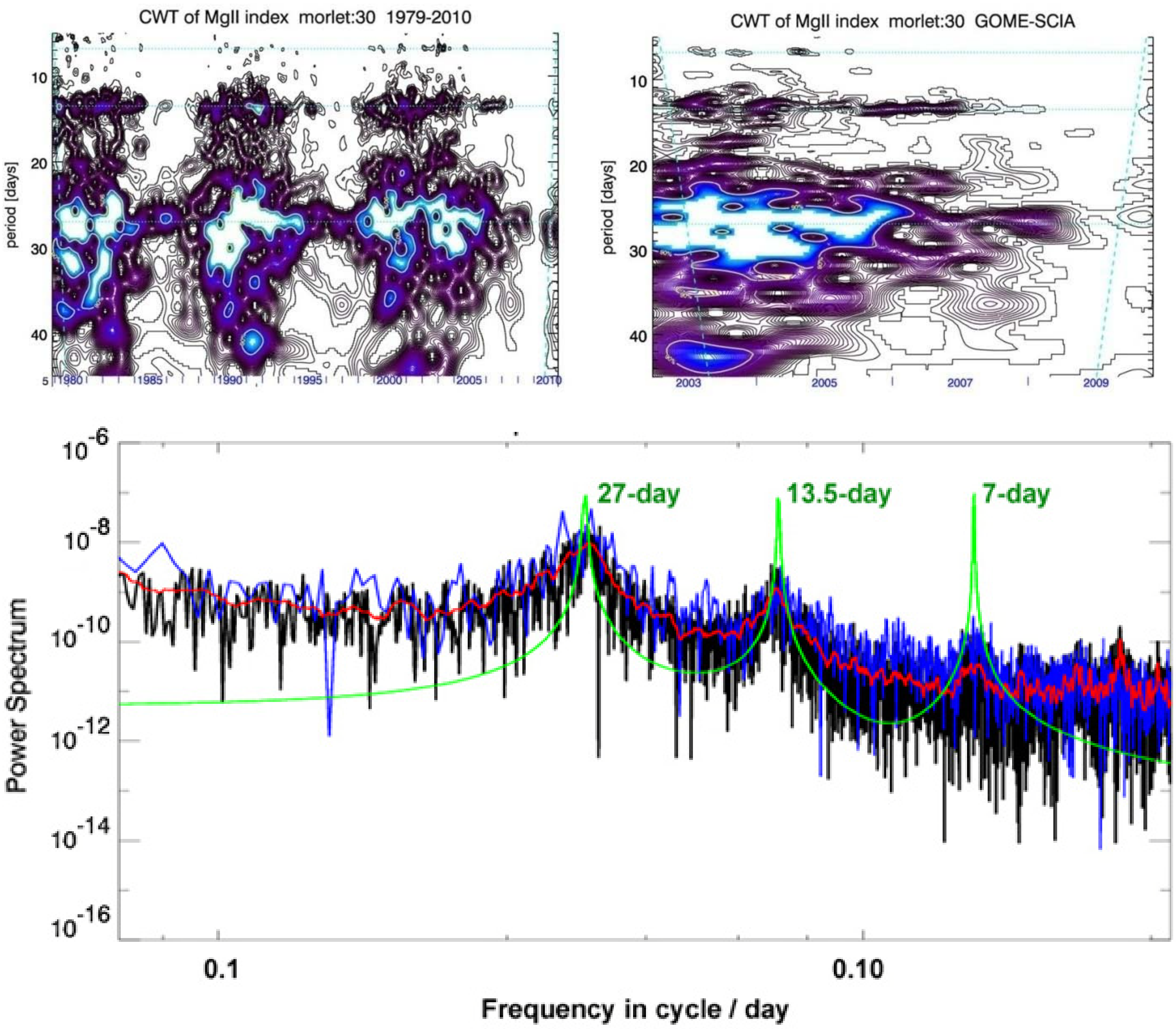

Fig 5.11. The 7-day periodic feature in CWT and FFT of final composite time series (black) and GOME-SCIA time series (blue). A supercomposition of three sinusoidal functions with periods equal to 27, 13.5, and 6.8 days is shown as a green line.

Although the wavepower at 7-day period scale in CWT plots does not reach the 90% significant level, still one can conclude that the small contours at this period scale are representing a periodic feature.

In the FFT plot, the black and blue colors represent the FFTs of the final composite time series and GOME-SCIA time series respectively, and the red line represents the smoothed composite power spectrum. We can obviously recognize the 7-day signature as a peak in both composite and GOME-SCIA time series. The green line corresponds to the FFT of an arbitrary function, which is a supercomposition of three sinusoidal functions with periods equal to 27, 13.5 and 6.8 days. The sinusoidal function with pre-defined 6.8-day period matches the 7-day signature best. Hence it can be assumed that the real period of this feature is less than 7 days and on the order of 6.8 days. This composite function was defined in this way:

$$f(x) = 0.004\left(sin\frac{2\pi x}{27} + sin\frac{2\pi x}{13.5} + sin\frac{2\pi x}{6.8}\right) \qquad equ.14$$

As it can be seen in the figure, the FFT of the arbitrary function is well matched with that of the two time series verifying the existence of all periodic features and most important, the 7-day (or 6.8-day) signature.

The finding of the 7-day signature was an unexpected outcome of this study. The physical phenomenon which is responsible for this periodic feature was not clear to the writer at the time of writing this thesis, but since it is a fourth harmonic of the solar rotational period and has a quadrupole effect, it is apparently related to the distribution of faculae on the solar surface, here 90° spacing.

Although the existence of the 7-day periodicity was suspicious to the writer at the beginning, the study done by Fioletov (Fioletov et al., 2009) verified the results of this work regarding the existence of the 7-day periodic feature by introducing a 6.7-day periodicity. The study by Fioletov also provides information on the influence of the 6.7-day periodicity on stratospheric ozone. Figure 5.12 (left panels) shows the power spectra of the three solar data sets for the time interval 1979–2005 and also SOLSTICE measurements at 205 nm estimated for the period from September 1991 to June 2000. The 6.7-day periodicity is clearly visible in the Mg II time series (left-bottom panel). The Mg II index also demonstrates the largest coherency with tropical stratospheric ozone time series (Fioletov et al., 2009). The coherency between ozone in layers 7–9 and the Mg II index time series can be seen in the right panel of Figure 5.12.

Another periodic feature which has been studied by Fioletov is the 9-day periodicity. From the figures, we can see that the amplitude of this periodic signature is much smaller than that of the 27, 13.5, and 6.7-day periodicities. Looking for this feature (which can be regarded as the third harmonics of the 27-day solar rotational period) was also one of the initial goals of this study, however it did not appear in the results. The reason might be the origin of this signature. The 9-day periodicity arises from a "triangular" distribution of coronal holes approximately 120° apart in solar longitude (Temmer et al., 2007). Since the Mg II is a proxy for monitoring the "chromosphere" temperature fluctuations and basically has nothing to do with coronal events, it is understandable why the 9-day signature is not well recognizable in the results.

As a brief summary, the 27-day rotation cycle of the sun generates a combination of different periodicities in solar UV flux known as harmonics. These periodicities have been investigated by analyzing the Mg II index time series as a proxy of solar UV flux variations. Although this study was begun to specifically reveal the 13.5 day periodicity, the detection of the 7-day periodic feature was a significant unexpected outcome of this study.

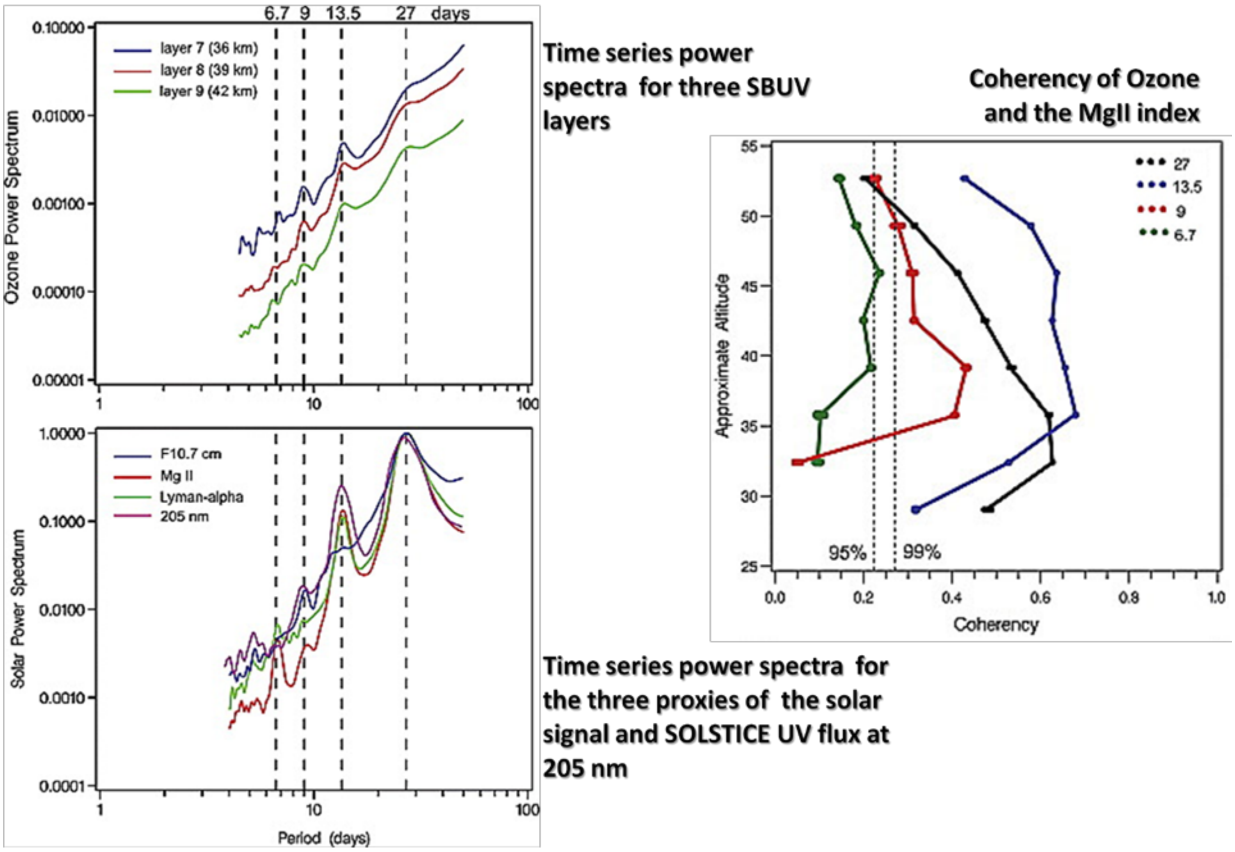

Fig. 5.12. (top-left) Ozone power spectra for three SBUV layers as indicated for the period 1979–2005. (bottom-left) Time series power spectra for the three proxies of the solar signal: Mg II index, the solar flux at 10.7 cm, and composite solar Lyman alpha estimated for the period 1979–2005 and for SOLSTICE UV flux at the 205-nm data set estimated for the period from September 1991 to June 2000. The solar spectra are normalized to the 27-day period value. The vertical lines indicate the 27-, 13.5-, 9-, and 6.7-day periods. (right) Coherency of ozone and the Mg II index for the 27-, 13.5-, 9-, and 6.7-day periods as a function of altitude (Fioletov et al., 2009).

5.3. Summary

The data from ten Mg II core-to-wing data sets have been combined into a single 32-year Mg II Index. The number of data sets and the quality of the data allow the creation of a single time series that captures both the short-term variability as well as the long-term trends. We have shown in this study that the correlation between various Mg II data sets is extremely good and that scaling the data to a common scale is quite reasonable. Furthermore, we have selected key data sets as the references to represent the overall trends in the final composite Mg II index. The remaining data are used to fill in data gaps. For days when no Mg II data are available, we have used F10.7 cm solar radio flux data to fill data gaps. In this way we have created a continuous uninterrupted record of the Mg II core-to-wing ratio that spans the period from November 1978 to June 2010. The Mg II time series also reveals the starting of the solar cycle 24. Having the composite Mg II time series, it is possible to apply different analytical methods to investigate the short-term periodic features of the solar UV variability. The FFT and WT methods have been used for this purpose. For extracting the short-term periodic features using WT, we have used Morlet wavelet with a high wavelet parameter in order to increase the resolution in the frequency domain. Both the FFT and WT of the Mg II index time series clearly show the 27 and 13.5-day periodicities as well as a weak 6.8-day periodic signal. The origin of the 13.5-day signature is the existence of a double hotspot system on the photosphere with longitudinal difference of 180°. The origin of the 6.8-day periodicity is not clear to the author. Although the amplitude of the 13.5 and 6.8-day signature is relatively low, but according to a study done by Fioletov (2009) the can have significant effect on ozone chemistry in the stratosphere.

References:

1. Bai, T. (2003), Hot spots for solar flares persisting for decades: ***Longitude distributions of flares of cycles 19–23;*** *Astrophys. J., 585, 1114–1123, doi:10.1086/346152 (2003)*

2. Berdyugina, S. V.: ***Preferred longitudes in solar and stellar activity;*** *Mem. Soc. Astron. Ital., 78, 242–246. (2007)*

3. Brueckner, G. E., K. L. Edlow, L. E. Floyd, J. L. Lean, and M. E. VanHoosier: ***The Solar Ultraviolet Spectral Irradiance Monitor (SUSIM) experiment on board the Upper Atmospheric Research Satellite (UARS)****; J. Geophys. Res., 98, 10,695 -- 10,711. (1993)*

4. Cebula, R.P., and M.T. DeLand,: ***Comparisons of the NOAA11 SBUV/2, UARS SOLSTICE, and UARS SUSIM MgII solar activity proxy indices;*** *Sol. Phys. 177, 117-132 (1998)*

5. Donnelly, R. F., L. C. Puga, J. Barrett, S. D. Bouwer, J. Pap, D. E. Stevens, and W. K. Tobiska: ***Solar UV flux measurements from the SBUV2 monitor on the NOAA-9 satellite: Part 1. Mg II h and k line core-to-wing ratios for 1986 – 1988****; NOAA Tech. Memo. ERL SEL-85, 211 pp., Natl. Oceanic and Atmos. Admin., Boulder, Colo. (1994)*

6. Fioletov V.E.: ***Estimating the 27-day and 11-year solar cycle variations in tropical upper stratospheric ozone****; JOURNAL OF GEOPHYSICAL RESEARCH, VOL. 114, D02302, doi:10.1029/2008JD010499, (2009)*

7. Floyd, L. E., P. A. Reiser, P. C. Crane, L. C. Herring, D. K. Prinz, and G. E. Brueckner: ***Solar cycle 22 UV spectral irradiance variability: Current measurements by SUSIM UARS****; Sol. Phys., 177, 79-- 87. (1998)*

8. Heath, D. F., and B. M. Schlesinge: ***The Mg 280 nm doublet as a monitor of changes in the solar ultraviolet irradiance;*** *J. Geophys Res., 91, 8672-- 8682. (1986)*

9. Rodney A. Viereck, Linton E. Floyd, Patrick C. Crane, Thomas N. Woods, Barry G. Knapp, Gary Rottman, Mark Weber5 Lawrence C. Puga, Matthew T. DeLand: ***A composite Mg II index spanning from 1978 to 2003****; SPACE WEATHER, VOL. 2, S10005, doi:10.1029/2004SW000084, (2004)*

10. Rottman, G. J., T. N. Woods, and T. P. Sparn***: Solar Stellar Irradiance Comparison Experiment 1: 1. Instrument design and operation;*** *J. Geophys. Res., 98, 10,667 -- 10,678.(1993)*

11. Temmer, M., B. Vršnak, and A. M. Veronig, ***Periodic appearance of coronal holes and the related variation of solar wind parameters;*** *Sol. Phys., 241, 371–383, doi:10.1007/s11207-007-0336-1. (2007)*

12. Thuillier, G., and S. Bruinsma: ***The Mg II index for upper atmosphere Modeling;*** *Ann. Geophys., 19, 219-- 228. (2001)*

13. Usoskin, I. G., S. V. Berdyugina, and J. Poutanen, ***Preferred sunspot longitudes: Non-axisymmetry and differential rotation;*** *Astron. Astrophys., 441, 347–352, doi:10.1051/0004-6361:20053201. (2005)*

14. Viereck, R. A., and L. C. Puga : ***The NOAA Mg II core-to-wing solar index: Construction of a 20-***

year times series of chromospheric variability from multiple satellite;*, J. Geophys. Res., 104, 9995- 10,005. (1999)*

15. Weber, M.,: ***Solar activity during solar cycle 23 monitored by GOME;*** *Proc. European Symposium on Atmospheric Measurements from Space (ESAMS'99), ESTEC, Noordwijk, The Netherlands, 18-22 January 1999, WPP-161, European Space Agency, p. 611-616 (1999)*

16. Zhang, L. Y., Y. M. Cui, Y. L. He, H. He, Z. L. Du, R. Li, and H. N. Wang: ***Longitudinal distribution of major solar flares during 1975–2005;*** *Adv. Space Res., 40, 970–975, doi:10.1016/ j.asr.2006.12.052. (2007)*